1-1-2004

A spectroscopic study of the star -forming properties of the center of Ngc 4194

Mark Hancock
University of Nevada, Las Vegas

NOTE TO USERS

A SPECTROSCOPIC STUDY OF THE STAR-FORMING PROPERTIES OF THE CENTER OF NGC 4194

by

Mark Hancock

Bachelor of Science
Northern Arizona University
1998

Master of Science
University of Nevada Las Vegas
2001

A dissertation submitted in partial fulfillment
of the requirements for the

Doctor of Philosophy Degree in Physics
Department of Physics
College of Sciences

Graduate College
University of Nevada, Las Vegas
May 2005

UNLV
UNIVERSITY OF NEVADA LAS VEGAS

Dissertation Approval

The Graduate College
University of Nevada, Las Vegas

03/04, 2005

The Dissertation prepared by

Mark Hancock

Entitled

A Spectroscopic Study of the Star-Forming Properties of the Center of NGC 4194

is approved in partial fulfillment of the requirements for the degree of

Doctor of Philosophy in Physics

Examination Committee Chair

Dean of the Graduate College

Examination Committee Member

Examination Committee Member

3/4/05

Graduate College Faculty Representative

PR/1017-52/1-00

ABSTRACT

A Spectroscopic Study of the Star-Forming Properties of the Center of NGC 4194

by

Mark Hancock

Dr. Donna Weistrop, Examination Committee Chair
Professor of Physics
University of Nevada, Las Vegas

We have obtained STIS longslit spectra of the central region of the advanced merger NGC 4194. The spectra cover the wavelength ranges 1150-1750Å in the UV and 2900-10270Å in the visible. Results from the study of the properties of 14 star forming regions (knots) are presented. We determine the average E(B-V)=1.1 mag using the combined Hα+[N II] flux. If the [N II] contribution is 40% then the average E(B-V)=0.7 mag. The metal abundances are found to be approximately solar. The average abundances calculated range from 8.1 ± 0.5 to 8.9 ± 0.1. The Hα luminosities of the 14 observed knots yield a total SFR of ~ 46 $M_\odot$ yr^{-1}. The sizes of the H II regions in the knots were determined from L(Hβ) and range from ~ 28 pc to ~ 119 pc when a filling factor of 0.1 is assumed. The sizes are a factor of ~ 2.15 smaller when a filling factor of 1 is assumed. Using Starburst99, and the EW(Hα+[N II]) and EW(Hβ), we estimate the ages of the star forming regions to be 5.5-10.5 Myr. From ground based spectra, the effective temperatures of the H II regions were found to be $\sim 11,000$ K and the electron densities were determined to be ~ 530 cm^{-3}. We find

that 8 of the knots likely formed with a Salpeter Initial Mass Function truncated at an upper mass of 30 $M_{\odot}$ and that one of the knots likely formed with a standard Salpeter Initial Mass Function. We find that the knots formed with a median SFE$\approx$18%. The knots in our sample have stellar masses in the range $\sim 0.6\times10^{6}$ $M_{\odot}$ up to $\sim 27\times10^{6}$ $M_{\odot}$. We suggest that the knots in our sample are likely the precursors of globular clusters.

TABLE OF CONTENTS

LIST OF TABLES

LIST OF FIGURES

ACKNOWLEDGEMENTS

Those who know me know that I am not especially good at this sort of thing. To acknowledge truly everyone that has made a difference in this project or my life would take more time and space than is allotted. Several people in my life have been supportive of my journey through graduate school. In particular, I would like to mention my fiancee Alexi Stone, my parents, Gary and Lorna Hancock, and my soon to be father-in-law John Stone. Several of my fellow graduate students made graduate school a much better experience. I would like to bring attention to Dr. Sandip Thanki and Mr. Greg Piet. I would like to thank the members of my Ph. D. committee, Dr. Spight, Dr. Lepp, and Dr. Reiber. Finally, I will thank John Kilburg and Dr. Selser.

That brings me to my advisor Dr. Weistrop who gave me an opportunity at a time when no one else would. Thank you.

You all know that I could not have done this without you. I want you all to know that I know it too. ;−)

CHAPTER 1

INTRODUCTION

Introduction

Recent observations indicate galaxy interactions can induce bursts of star formation. The role interactions play in galaxy evolution can be investigated in part by observing merging starburst galaxies, such as NGC 4194. Many interacting systems and merger remnants have been studied in optical and infrared wavelength regions (e.g. NGC 4038/4039 Whitmore *et al.* (1999), NGC 7252 Miller *et al.* (1997), NGC 3921 Schweizer *et al.* (1996), and references therein). Typically, the young clusters have radii of ≤ 5 pc, ages ranging from $1 - 10$ Myrs and cluster luminosity functions that can be fit with power laws with exponents ≈ -2 (Whitmore, 2003).

Observations in the ultraviolet are ideal to investigate the young star forming regions since in this wavelength range hot, young stars dominate the spectral energy distribution and can be easily distinguished from older populations. Ultraviolet observations prior to HST achieved angular resolutions of $\geq 1''$ (e.g., Hill *et al.* (1992), Kinney *et al.* (1993), Reichen *et al.* (1994), Deharveng *et al.* (1994)). With HST we can observe in the UV with ~ 50 mas (milliarcsecond) resolution (e.g., Conti & Vacca (1994), Meurer *et al.* (1995) and Johnson *et al.* (1999)), enabling us to observe individual star forming knots in external galaxies.

Several authors have proposed that the bright young star forming regions are the precursors of globular clusters (e.g., Whitmore *et al.* (1993), and Schweizer *et al.* (1996)). Ashman & Zepf (1992) suggested that globular clusters can be formed by

the interaction or merging of galaxies. Schweizer *et al.* (1996) put forth the idea that the formation of globular clusters and the origin of galaxy shapes might not be two separate problems. Evidence suggests that Hubble's morphological sequence might actually rank galaxies by the types and intensity of mergers (Schweizer *et al.*, 1996). Schweizer *et al.* (1996) also suggest that most mergers involve galaxies with gas. Such mergers might often lead to bursts of star formation. Entire systems of globular clusters might form as part of such a starburst (Ashman & Zepf, 1992).

Investigating young clusters also allows the study of massive stars, which are relatively rare and short lived compared to less massive stars. How often do very massive, > 30 $M_{\odot}$, stars form? Are the star forming efficiency and upper mass cutoff of the initial mass function correlated? Do the extreme star forming environments of galaxy mergers provide conditions conducive to the formation of massive stars?

Our data were taken with the STIS, Space Telescope Imaging Spectrograph, on board the Hubble Space Telescope. Three sets of long-slit spectra were taken to cover the wavelength ranges of 1150-1730 Å in the FUV and 2900-10270 Å in the visible. The data were taken using three long-slit gratings, G140L, G430L, and G750L and are centered at 1425 Å, 4300 Å, and 7751 Å, respectively.

Using the spectral synthesis models, Starburst 99, we estimate the ages and masses of the star forming regions in NGC 4194. We also derive the luminosities, reddening, metallicities, redshift, star formation rates and star formation efficiencies of the knots. Finally, we constrain the upper mass cutoff to the IMF of the star forming knots. We compare our spectroscopic results with recent imaging results on NGC 4194 by Weistrop *et al.* (2004). We also compare the properties of the star forming regions in NGC 4194 to globular clusters in the Milky Way and to nearby interacting galaxies.

Knot Characteristics

What is a knot? A knot is a star forming region, a group of very young stars. Other authors refer to knots as star clusters, or even super star clusters. We use the term knot. Knots are observed in galaxies undergoing intense bursts of star formation. Some such galaxies are interacting or merging. Tidally induced shocks compress gas that forms knots in the outer regions of interacting galaxies. Sometimes in a merger gas will fall to the center of the galaxy and induce star formation there. Typically knots are observed with ages less than 20 Myr and some as young as a few Myr. The knots can have sizes ranging from a few parsecs (pc) to tens of pc. For now, stars in the knots observed in galaxies other than our Milky Way or the LMC and SMC are not resolved. Over time some of the stars in a system may be ejected from the knot due to stellar encounters. Some of these star forming regions are gravitationally bound and will likely become open or globular clusters. The rest of the knots are probably OB associations, a group of unbound stars that will eventually dissipate. Knots typically contain on the order of 10^5 to 10^6 $M_\odot$ of newly formed stars. The stars are initially distributed by mass according to an initial mass function (IMF). It is thought that the IMF takes the form of the Salpeter IMF, $\Phi(M) = cM^{-2.35}$, where the mass units are in solar masses and c is a normalization constant. A knot with this IMF could contain stars ranging in mass from as high as perhaps 100 $M_\odot$ down to as low as 0.1 $M_\odot$ or even less. A 10^6 $M_\odot$ knot formed according to a Salpeter IMF would contain around 5 O3 stars, 150 B0 stars, 15,000 A0 stars, 60,000 F0 stars, 160,000 G0 (similar to our sun) stars, 310,000 K0 stars, and 870,000 low mass M0 stars. These stars range in surface temperature from the most massive O stars at 50,000 K to the low mass M stars at 3000 K. Each of these stars is approximately a black body. Figure 1 is a plot of the approximate contribution of each spectral type in a knot to the composite spectrum assuming a Salpeter IMF from 0.1 to 100 $M_\odot$.

From this plot the contributions of the stars of different masses to different parts of the spectrum can be seen. The O and B stars dominate the emission at wavelengths less than 2000 Å. In the visible spectrum, around 5500 Å, G and K stars contribute the most intensity. The low mass red M stars, of which there are 870,000, dominate the spectral energy distribution in the infrared at wavelengths greater than 10,000 Å, although the K stars are also important.

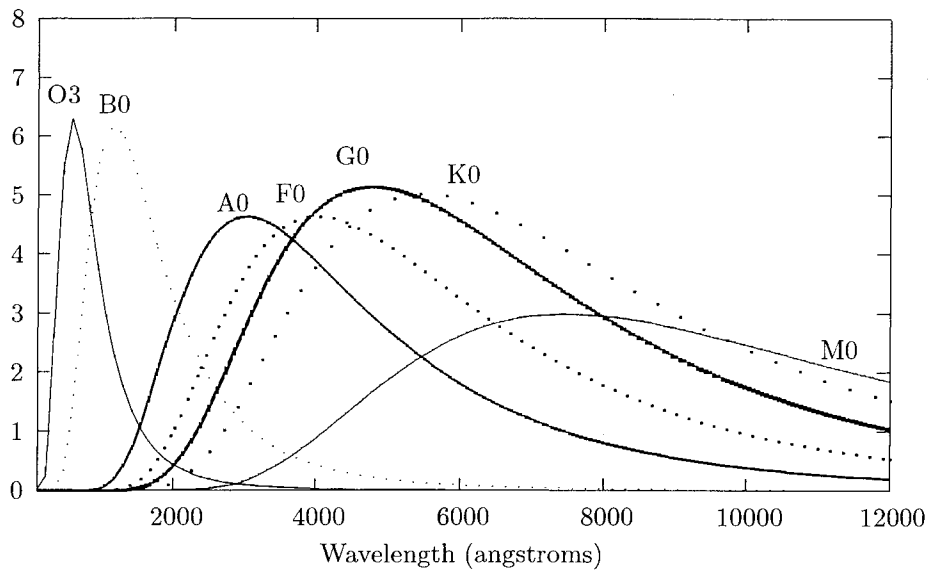

Figure 1 Spectral Energy Contributions. The vertical axis is Intensity in arbitrary units

A knot is not just stars. These stars form in great clouds of gas. The gas gravitationally collapses and when a particular clump becomes sufficiently hot and dense enough in the center, nuclear fusion occurs. We have a star. Not all the gas in the region is taken up by stars. The young stars are surrounded by gas. They are embedded in it. The gas is mostly hydrogen. Other elements that make up the gas include helium, oxygen, nitrogen, and sulfur. The ionization potential for hydrogen is 13.6 eV, corresponding to 912 Å. From Wien's displacement law, $\lambda_{max}T = 0.290$ cm K, a 30,000 K star will have its peak emission at 966 Å. So the UV radiation from the O and B stars will ionize hydrogen. The ionization zone, or H II region, will extend

out a few pc from the stars. Outside the H II region is a gas of neutral hydrogen and the other elements mentioned previously. The electron densities of the ionized gas in these regions are typically a few hundred per cubic centimeter. The electron temperature of the gas is usually around 10,000 K.

If a knot contains sufficiently massive stars, a third possible component is the stellar wind. According to one scenario, stars more massive than around 25 $M_{\odot}$ will become Wolf-Rayet stars (Conti (1976), Massey (2003)). These Wolf-Rayet stars and regular O stars eject mass, due to the intense outward flow of radiation combined with the stars' low surface gravity. This ejected mass is the stellar wind. Kroupa (2002) says that stellar winds of 100-1000 km s^{-1} are typical and that an O star can lose up to 10% of its mass during its main sequence lifetime. The presence of these stellar winds influences the development of the knot. It is believed that the small and intermediate mass stars form first. The star formation is thought to stop once the most massive stars form (Herbig (1962), Massey (2003)). When the massive stars are only a few Myr old, the stellar winds will blow out the gas, leaving nothing from which to form more stars. Once the massive stars attain ages of $\sim$ 5 Myr, supernova explosions will disrupt the gas (Massey, 2003). Massive stars can be detected by the presence of stellar wind lines in the spectra.

All three components of a knot can be seen in the spectra. The stars produce the continuum and some absorption lines. The nebulae or H II regions produce emission lines in the visible, for example the Balmer lines and forbidden lines like oxygen. The densities in the gas are low enough that an atom can be collisionally excited and will not be collisionally de-excited before it emits a photon and goes to a lower energy level. The stellar winds can be observed in the UV as components of absorption lines of metals like carbon and silicon.

CHAPTER 2

OBSERVATIONS

Instrumentation

The 2.4 meter Hubble Space Telescope (HST) was deployed in low-Earth orbit, $\sim$ 600 km, by the crew of the space shuttle Discovery on April 25, 1990. The Space Telescope Imaging Spectrograph (STIS) was installed in 1997. The STIS spectrograph provides several spectroscopic modes, including long-slit, echelle, and prism. STIS uses three 1024x1024 pixel detectors to span wavelengths from 1150-11000Å. The visible wavelength detector is a charge coupled device (CCD), and the two ultraviolet detectors are multi-anode micro-channel arrays (MAMA) (Woodgate *et al.*, 1998).

In short, a CCD detector works when incident photons hit a semi-conducting surface, usually doped silicon, and excite electrons. The electrons are trapped in a potential. Charge accumulates in that potential during the exposure time and is linearly proportional to the number of incident photons. At the end of an exposure the charge is read out. The CCD detector covers a wavelength range from 2000-11000Å. The CCD has a $52'' \times 52''$ field of view (FOV) and a $0.0507''$/pixel scale. The pixels are $21 \times 21\mu$m in size (Woodgate *et al.*, 1998).

The two MAMA detectors work differently. Photons strike the photocathode, liberating single electrons which pass into the micro-channel plate. There they are multiplied to a pulse of $\sim 4 \times 10^5$ electrons. The pulse is recorded by an anode array behind the photocathode. The pulse is then detected by the MAMA electronics and processed to determine the location of the photon event on the detector (Woodgate *et*

al., 1998). One MAMA detector covers the wavelength range in the near ultra-violet (NUV), 1600-3100Å. The other covers the wavelength range in the far ultra-violet (FUV), 1150-1700Å. The MAMA detectors have a 0.0247″/pixel scale with $25 \times 25 \mu$m pixels. The FOV is 25″ × 25″ (Woodgate *et al.*, 1998)

The STIS spectrograph was designed to observe at low, medium and high dispersions. Low dispersion observations are made through first order gratings. The three gratings we used for our low dispersion observations were the G140L, G430L, and G750L. The G140L has an average dispersion of 0.6Å/pixel. The G430L has an average dispersion of 2.73Å/pixel. The G750L has an average dispersion of 4.92Å/pixel.

Observations

Table 1 Observation Log

ID	Detector[a]	Grating	$\lambda_{central}$ (Å)	Range (Å)	Exposure[b] (sec)	Date (UT)
o5fy01010	MAMA	G140L	1425	1150-1730	2422	09/16/1999
o5fy01020	MAMA	G140L	1425	1150-1730	3071	09/16/1999
o5fy01030	CCD	G430L	4300	2900-5700	1489	09/16/1999
o5fy01040	CCD	G750L	7751	5240-10270	1080	09/16/1999

[a]MAMA=Multi Anode Microchannel Array, CCD=Charge Coupled Device.
[b]FUV images were combined. Weighted exposure time is 2785 seconds.

Four long-slit spectra covering three wavelength ranges were taken of the center of NGC 4194 with STIS. The observations were taken during cycle 8 under proposal ID 8032. Table 1 is the observation log. Column 1 lists the data ID's, column 2 shows the detectors that were used, column 3 lists the gratings that were used, column 4 shows the central wavelengths of the gratings, column 5 lists the wavelength ranges of the gratings, column 6 shows the exposure times, and column 7 lists the

UT observation dates. The $52'' \times 0.5''$ slit was centered at $12^h14^m9.41^s$ R.A. and $+54^o27'9.64''$ DEC. (J2000) and was oriented $-32^o.3443$ East of North for both CCD spectra and $-32^o.4002$ East of North on the FUV spectra. Figure 2 shows an HST CCD image of NGC 4194 with the approximate slit position.

The two FUV MAMA spectra were combined to increase the signal to noise ratio. The two images were averaged and weighted by exposure time. The final weighted exposure time was 2,785 seconds.

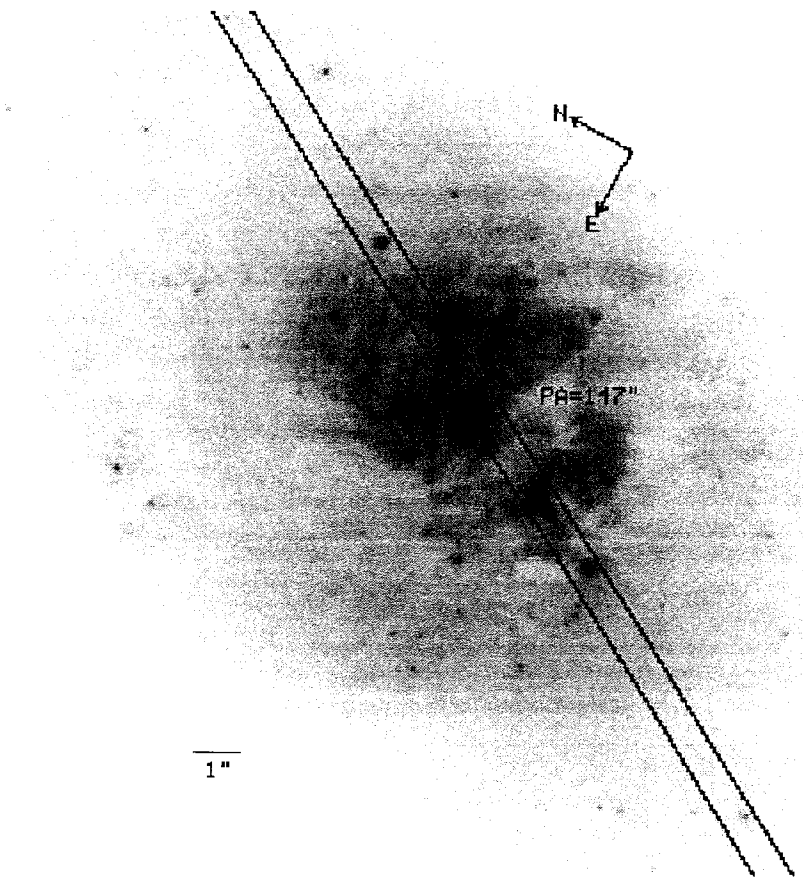

Figure 2 HST CCD image with slit location

Two Dimensional Spectra

The data one retrieves from the STIS long-slit configuration are two dimensional spectra. The horizontal axis is wavelength and the vertical axis is spatial. The slit length corresponds to the y axis. Light from individual sources along the 52″ slit is diffracted along the x axis. Figures 3-5 are examples of two dimensional spectra. The individual horizontal lines are the dispersed light from individual star forming regions. In Figure 3, Hα can be seen in emission. The Hα emission line extends beyond the various horizontal lines. The Hα line shows the extent of the nebular regions around the star forming knots while the horizontal lines are the continuous emission of the stars embedded in the nebula. In Figure 4, Hβ, [O III] λ4959, and [O III] λ5007 can be seen in the last third of the spectrum. The two large gaps in Figure 5 are geocoronal Lyα λ1216 and O I λ1302 emission lines that were removed and are discussed below. The various absorption features seen in Figure 5 include Si IV λ1403 and C IV λ1550 .

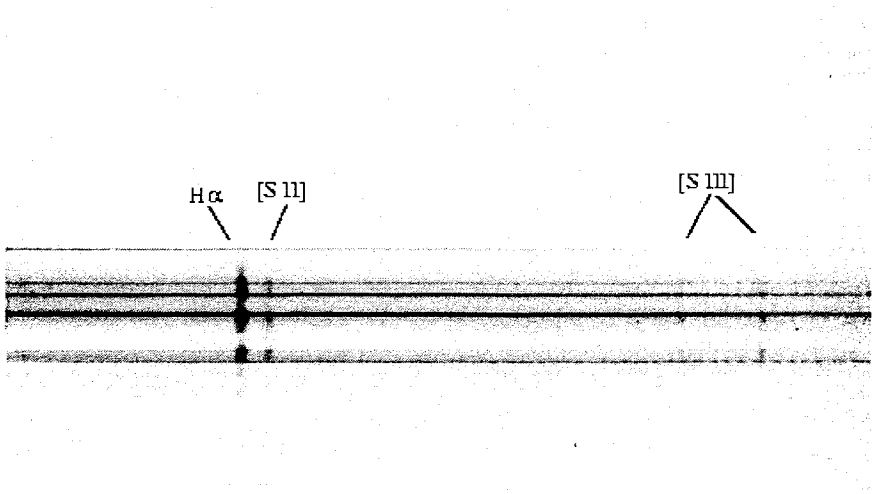

Figure 3 Example of 2D Spectra from G750L grating

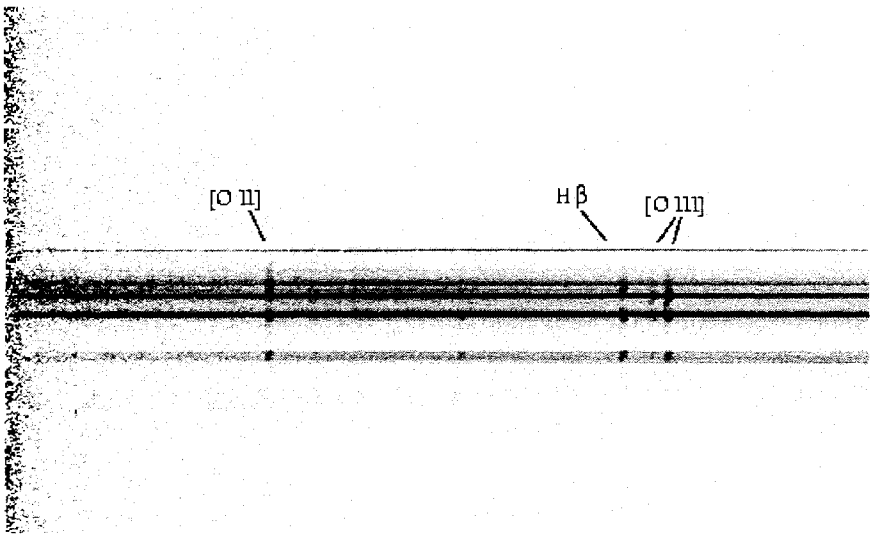

Figure 4 Example of 2D Spectra from G430L grating

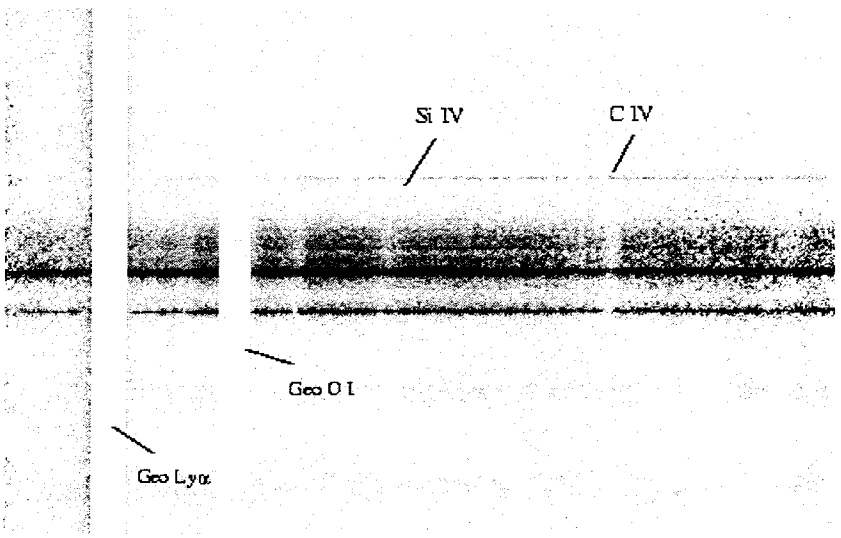

Figure 5 Example of 2D Spectra from G140L grating

CHAPTER 3

DATA REDUCTION AND CALIBRATION

Pipeline Reductions

The data were reduced in part with on-the-fly re-processing (OTFR) through the HST pipeline at STScI. This means that the most up-to-date reference files were used. The motivation for OTFR came from the scientific need to recalibrate data to take advantage of various improvements in calibration. Instruments that undergo an evolution of calibration files or calibration software often require that users carry out their own recalibrations. With OTFR, the STScI carries out the recalibration. The major reductions performed in the pipeline are the bias subtraction, the flat field correction, the dark current correction, the wavelength calibration and flux calibration. After OTFR, we received a set of reduced 2 dimensional flux calibrated spectra.

Bias subtraction is done to remove the charge electronically added to the pixels on the CCD detector. Information is retrieved from the CCD detector by transferring the charge in each pixel across the chip. A certain amount of charge is lost in that process. The charge transfer efficiency (CTE) is defined as the ratio of the charge read out to the original amount of charge in the pixels. The CTE is poor for small amounts of charge, so to ensure that there is enough charge for a good CTE, charge is electronically added to each pixel. This charge is the bias. A bias image is created by taking a zero second time exposure. The resultant image is only of the bias charge. Several of these are taken and then combined to form the final bias image. Then the final bias image is subtracted from the data image.

The flat field is divided into the data image to remove the effect of each pixel not being equally sensitive to photons of a particular wavelength. A flat field image is created by imaging a known uniform light source, typically a part of the sky during twilight if observing from the ground. From space, however, with STIS, flat fielding lamps are used. A tungsten lamp is used for the CCD detector and a krypton lamp is used for the FUV MAMA. All external light is blocked when the lamps are used for creating flat field images.

The dark frame is subtracted from the data images to remove hot pixels and thermal charge. On long integrations thermal charge can accumulate in the pixels due to the thermal effects in the detector. Hot pixels caused by radiation damage, such as cosmic rays, occur on the CCD detector but not on the MAMA detectors. Both the CCD spectra and the MAMA spectra have had the dark frames subtracted. The dark image is created by taking time exposures with the camera shutters closed. With no light entering the detector all that is in the images are the hot pixels, small amounts of accumulated thermal charge, and the bias charge, which is removed separately as described earlier.

Wavelength calibration is done because every time an exposure is taken with a different grating, the spectrum may be placed on a slightly different part of the detector. When the grating wheel or mode selection mechanism (MSM) is moved, the resulting spectrum is projected onto the detector with an error in location of $\leq \pm 3$ pixels (Woodgate *et al.*, 1998). An exposure is taken with the internal tungsten lamp following each use of a new grating. Using the known emission wavelengths of the tungsten lamp, a pixel offset is calculated. This allows the calibration of the zero point of the wavelength (dispersion) axis.

Flux calibration is done to convert the raw counts into fluxes with units ergs s^{-1} cm^{-2} $Å^{-1}$ $arcsec^{-2}$. The pipeline assumes a uniform point source illumination for the

flux calibration. This assumption has implications for the measurements of emission line fluxes, see the "Emission Line Strengths" section.

In-House Reductions

In addition to the standard pipeline procedures, a few more calibrations steps were implemented. These in-house reductions were all done with IRAF. The first additional reduction was to remove hot pixels that remained after the dark correction. The next calibration step was correcting the fringe effects on the long wavelength CCD spectra. The final reduction step was removing the geocoronal Lyα λ1216 and O I λ1302 lines. Following is a description of the in-house reductions.

To remove any remnant hot pixels, the COSMICRAYS task was used to scan the images 7x7 pixels at a time. Any pixel value over a predetermined threshold was replaced with the window average excluding that outlying value. We used a threshold of 5 standard deviations of the background. The data were then scaled by 10^{16}. This was done only as a display convenience. The units of each pixel were then 10^{-16} ergs s^{-1} cm^{-2} $Å^{-1}$ $arcsec^{-2}$.

Next we de-fringed the long wavelength CCD image. Longward of 7500Å fringing effects can be seen. At these wavelengths the photons are of the order of the thickness of the layers making up the CCD structure and can interfere. The fringe pattern is a convolution of the contours of constant distance between the front and back surfaces of the CCD and the wavelength of the light on a particular part of the CCD. The fringe pattern can be corrected with a contemporaneous flat field. The flat field used to correct the fringing was a tungsten lamp spectrum taken through the same grating wheel setting during the same orbit as our data. We used the NORMSPFLAT, MKFRINGEFLAT and DEFRINGE tasks to apply the contemporaneous flat correction to the data and remove the fringe pattern.

Next, we removed the strong geocoronal Lyα λ1216 and O I λ1302 emission lines from the UV spectra. HST is in a low Earth orbit and is sensitive to some atmospheric emission. An attempt was made to model and remove the Lyα λ1216 but no data from the galaxy was retrievable. The signal from NGC 4194 in the wavelength range around 1216Å was too weak in comparison to the geocoronal Lyα λ1216 .

One Dimensional Extraction

Once the two dimensional spectra were reduced and calibrated, we identified several spatial features and extracted one dimensional spectra of them. These spatial features are individual star forming regions, which we refer to as 'knots'.

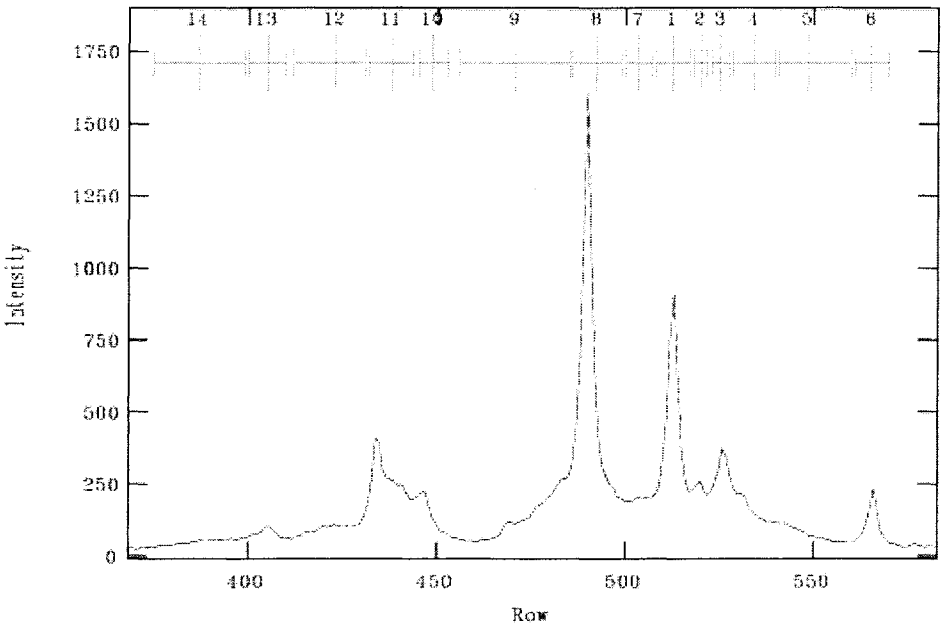

Figure 6 Aperture Placement. The emission features are individual star forming regions.

The apertures used to extract the one dimensional spectra were defined such that they had the same spatial extent in all three band passes. The apertures are the number of pixels in the spatial direction needed to encompass the individual

horizontal lines on the 2 dimensional spectra. This was done by plotting the intensity distribution along the spatial axis in all three band passes in regions with no significant line emission. In pixel coordinates the region plotted was centered at column 440 and was 40 pixels wide in the wavelength coordinate. The region was averaged over 40 pixels in the wavelength axis to gain a reasonable signal to noise ratio to facilitate knot identification. All three band passes were plotted in angular coordinates because the angular scales are different for the MAMA and CCD. We were then able to define apertures for each knot in those angular coordinates. The angular coordinates of each aperture were then converted to individual detector pixel coordinates. We forced the aperture definitions to be an integer number of pixels. A plot of the spatial dimension of the G750L spectra showing the apertures we defined can be seen in Figure 6. Table 2 shows the apertures we chose. A knot had to meet two criteria to be included. It had to be present in all three band passes and be at least 2 pixels ($\sim$ 19 pc) wide on the CCD detector and 4 pixels ($\sim$ 19 pc) on the MAMA detector. Knots 9, 12, and 13 have significantly less UV flux than visible flux.

Once the apertures were defined, we extracted the one dimensional spectra using the IRAF task APALL. The APALL task sums all the rows in each aperture and extracts them into one file per aperture. Because we wanted the average flux in each aperture and not the sum, we divided each one dimensional spectra by the number of pixels in its aperture. Finally, the noise spikes at the edges of each of the one dimensional spectra were removed for display convenience. Typically the regions removed corresponded to $\sim 30 - 75$Å, or 15-50 pixels. Care was taken to ensure that no measurable lines were in the regions removed.

Figures 7-20 are the extracted one dimensional spectra of the 14 knots. In several of the knots, the visible spectra show strong emission lines and an increase in the continuum toward blue wavelengths, indicating the presence of massive O, B, and A

Table 2 NGC 4194 Apertures

Knot	FUV MAMA G140L[a]	CCD G430L[a]	CCD G750L[a]
1	355-374	508-517	508-517
2	375-383	518-522	518-522
3	386-397	523-528	523-528
4	400-421	529-540	529-540
5	423-453	541-556	541-556
6	464-483	561-570	561-570
7	338-354	500-507	500-507
8	311-337	486-499	486-499
9	249-308	456-485	456-485
10	226-242	445-453	445-453
11	200-225	432-444	432-444
12	165-197	415-431	415-431
13	134-155	400-410	400-410
14	82-133	375-399	375-399

[a]aperture range in detector pixels.

stars. The bright UV continuum and strong C IV λ1550 and Si IV λ1403 absorption lines are also evidence for a young massive population.

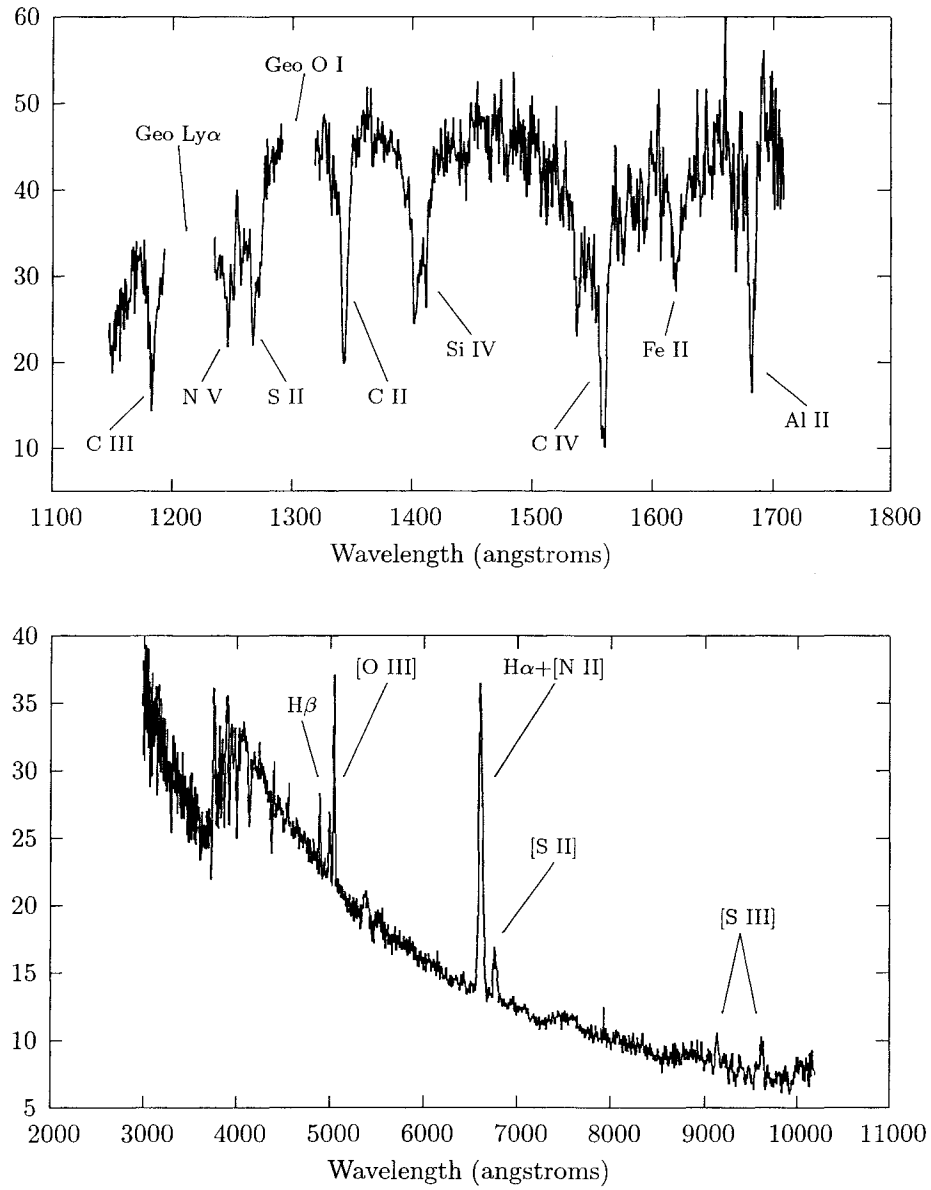

Figure 7 1D spectra of knot 1. The vertical axes are in units of 10^{-16} ergs s^{-1} cm^{-2} $Å^{-1}$ $arcsec^{-2}$

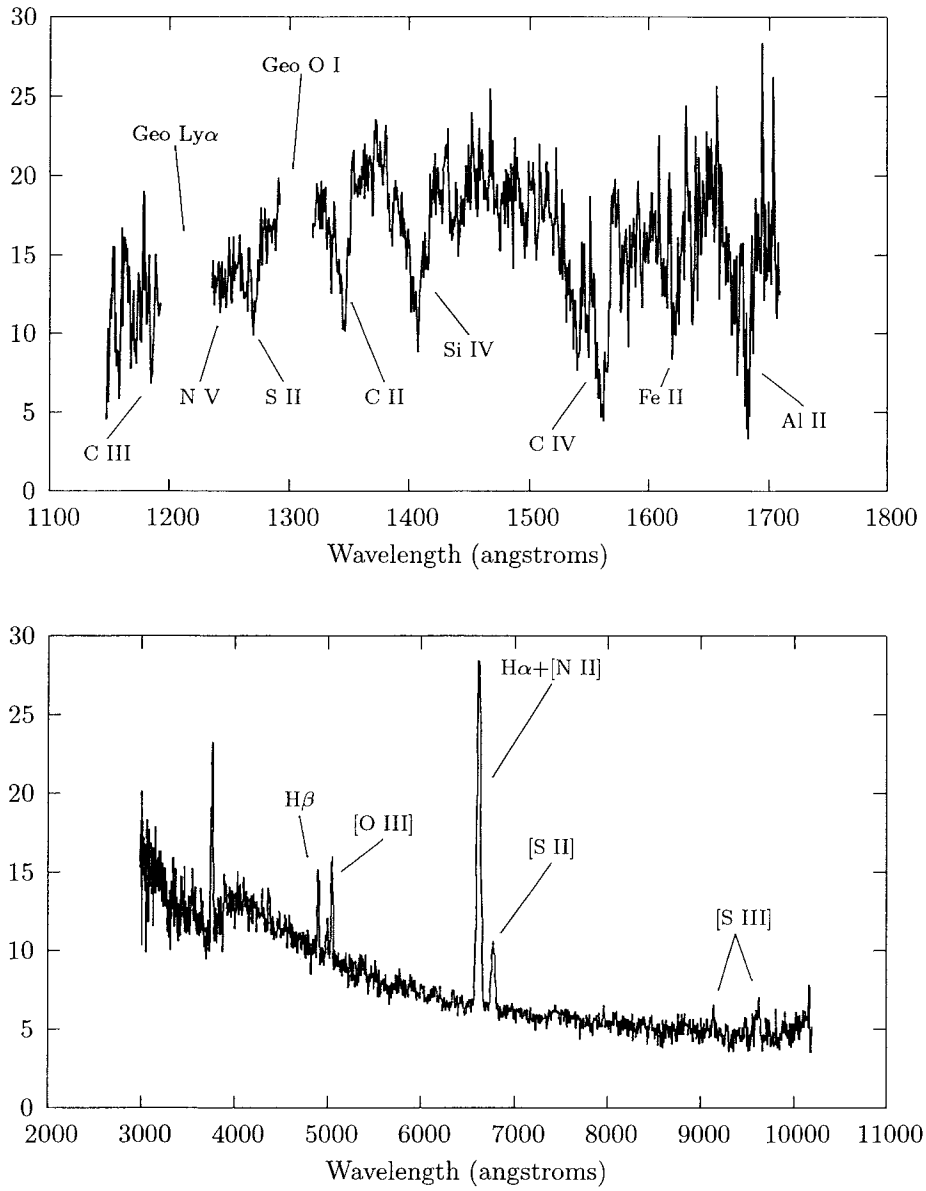

Figure 8 1D spectra of knot 2. The vertical axes are in units of 10^{-16} ergs s^{-1} cm^{-2} $Å^{-1}$ $arcsec^{-2}$

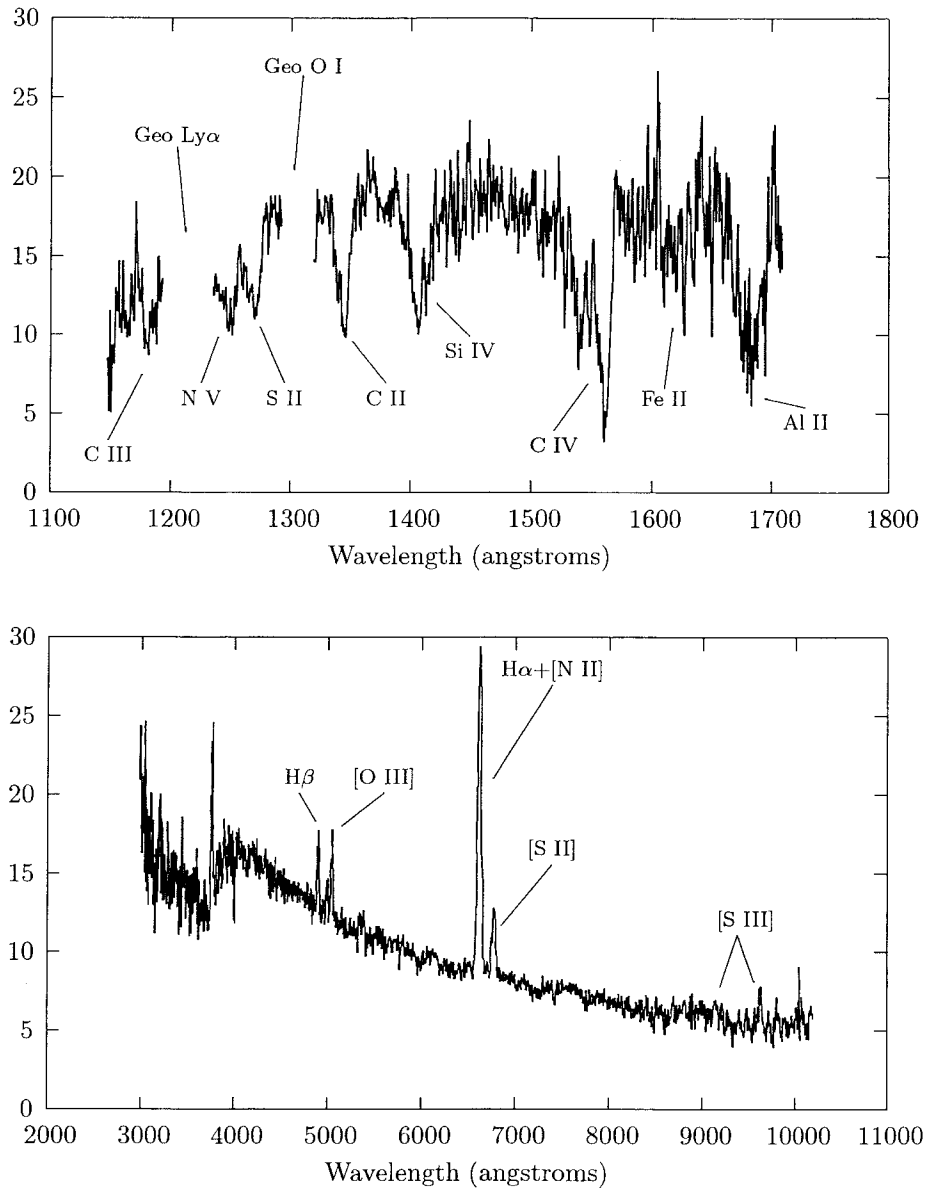

Figure 9 1D spectra of knot 3. The vertical axes are in units of 10^{-16} ergs s^{-1} cm^{-2} $Å^{-1}$ $arcsec^{-2}$

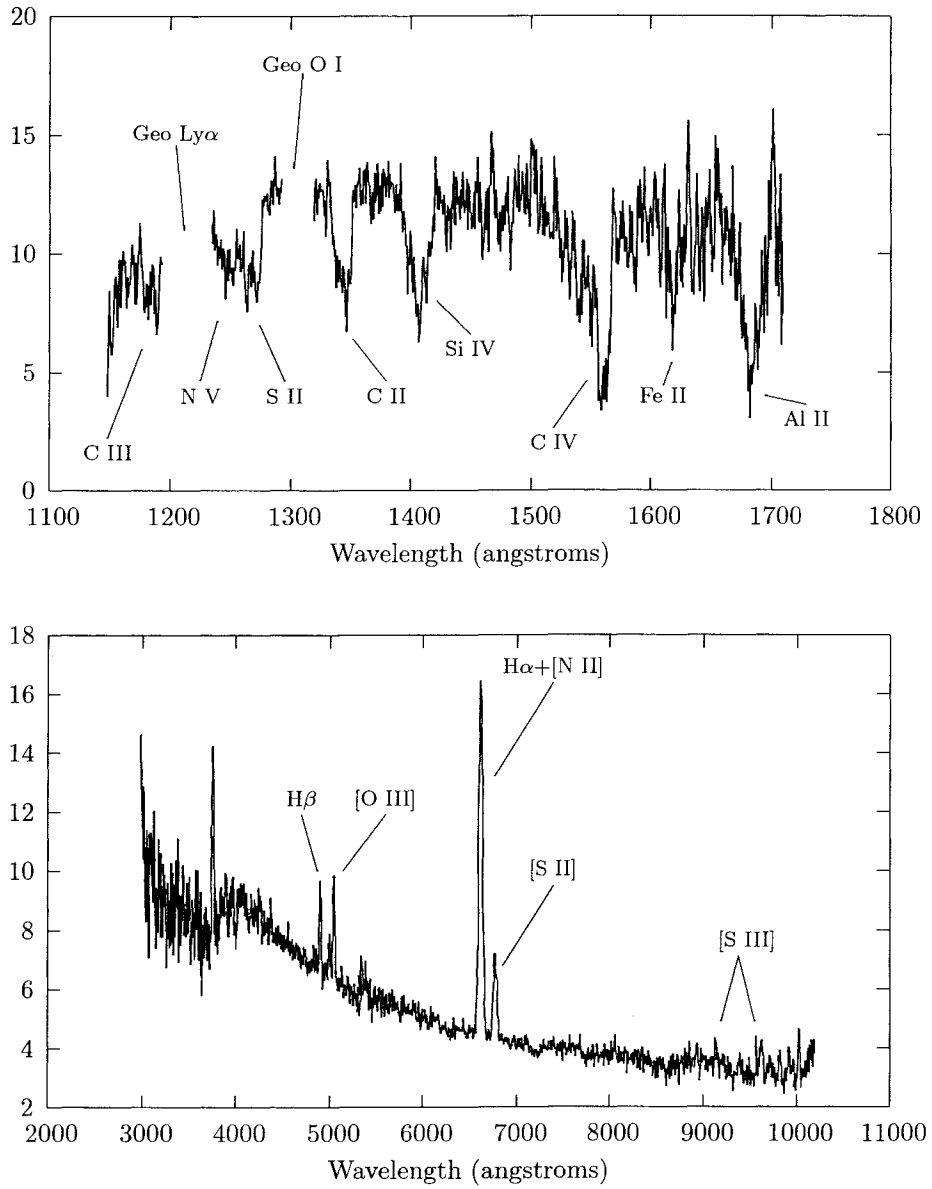

Figure 10 1D spectra of knot 4. The vertical axes are in units of 10^{-16} ergs s^{-1} cm^{-2} $Å^{-1}$ $arcsec^{-2}$

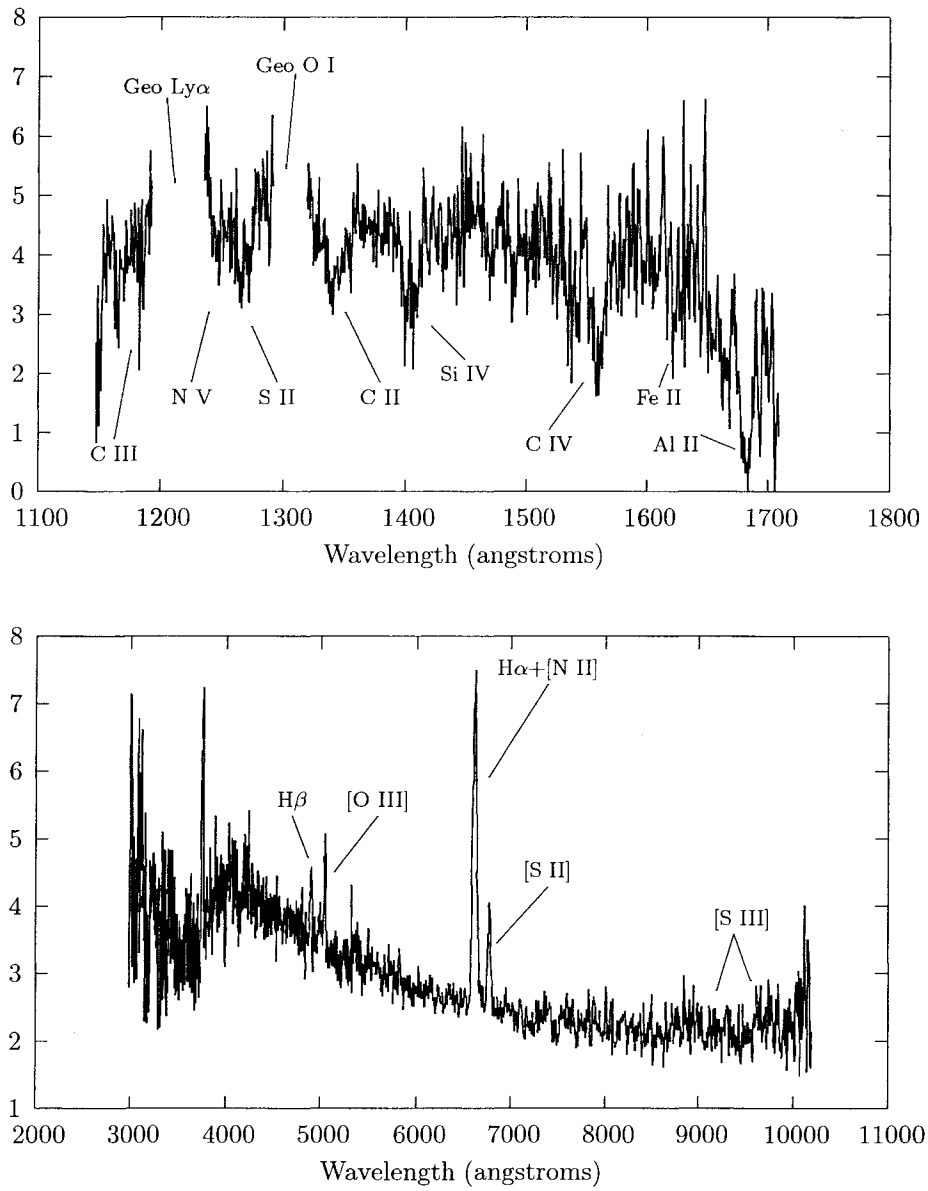

Figure 11 1D spectra of knot 5. The vertical axes are in units of 10^{-16} ergs s^{-1} cm^{-2} $Å^{-1}$ $arcsec^{-2}$

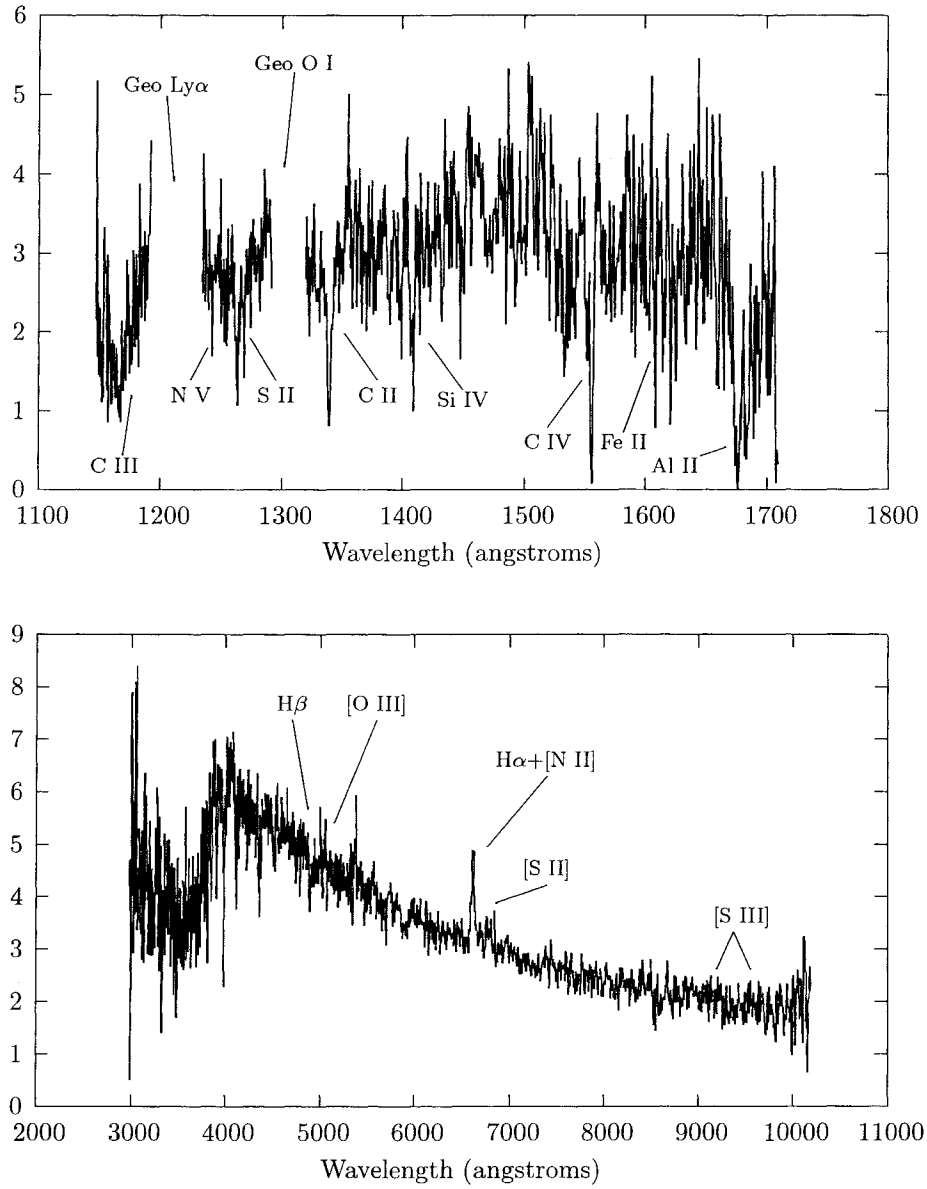

Figure 12 1D spectra of knot 6. The vertical axes are in units of 10^{-16} ergs s^{-1} cm^{-2} $Å^{-1}$ $arcsec^{-2}$

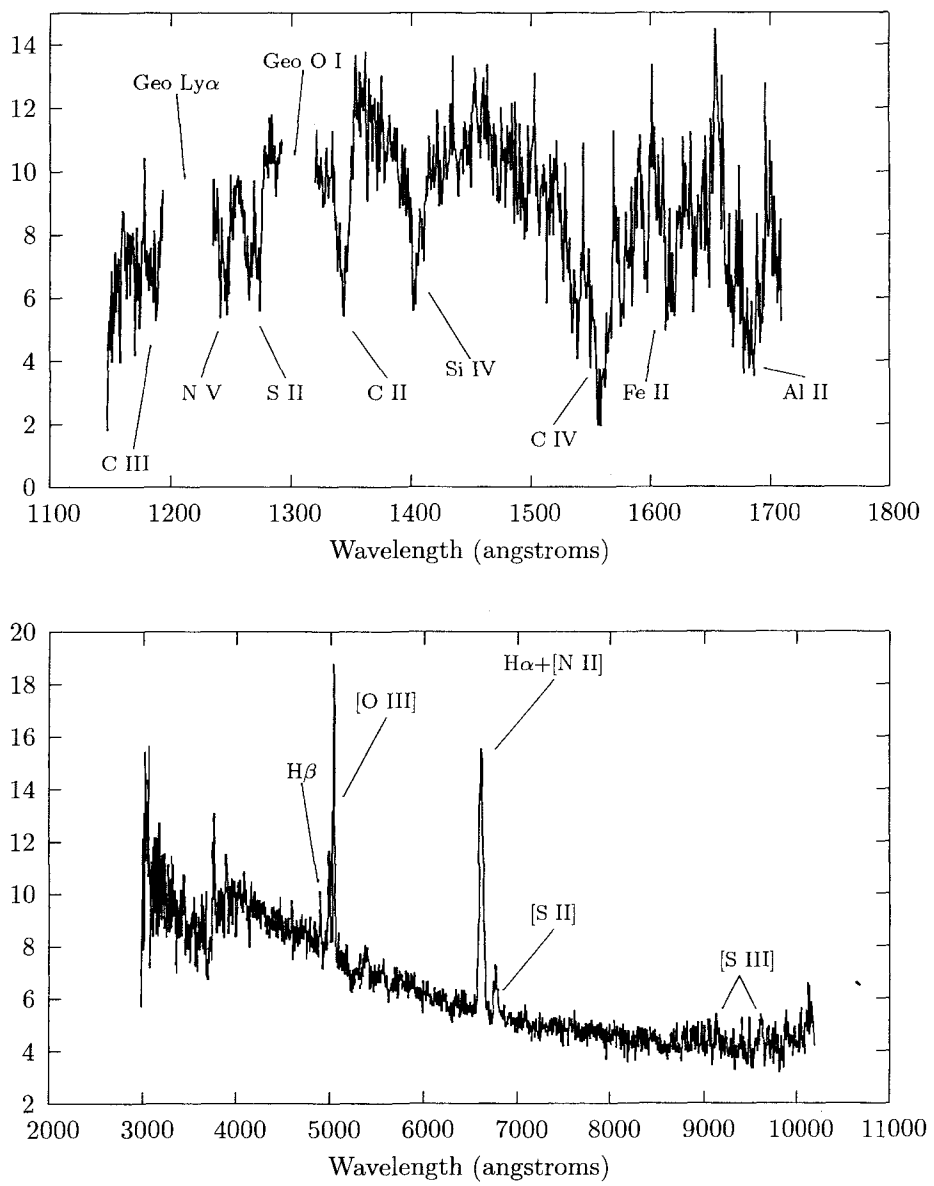

Figure 13 1D spectra of knot 7. The vertical axes are in units of 10^{-16} ergs s^{-1} cm^{-2} $Å^{-1}$ $arcsec^{-2}$

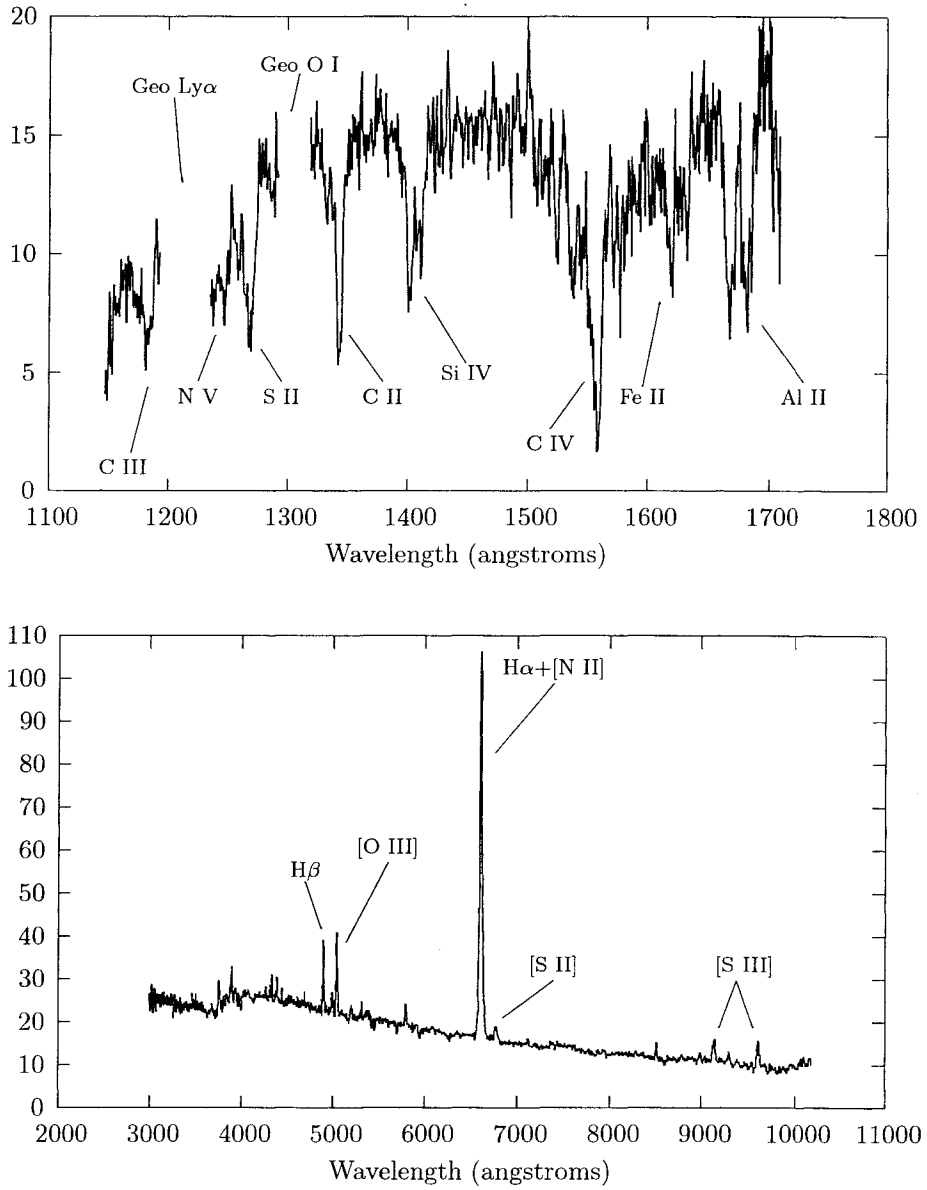

Figure 14 1D spectra of knot 8. The vertical axes are in units of 10^{-16} ergs s^{-1} cm^{-2} $Å^{-1}$ $arcsec^{-2}$

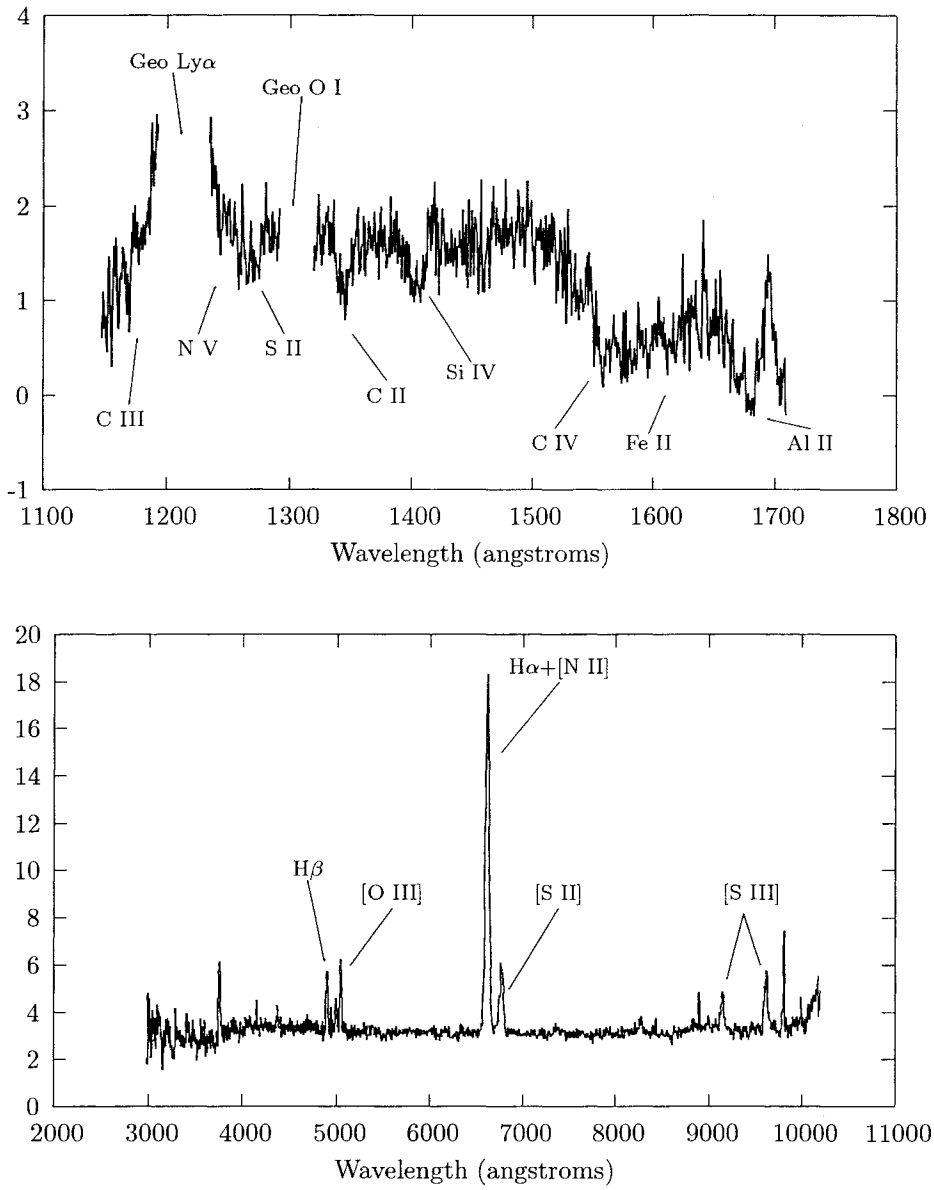

Figure 15 1D spectra of knot 9. The vertical axes are in units of 10^{-16} ergs s^{-1} cm^{-2} $Å^{-1}$ $arcsec^{-2}$

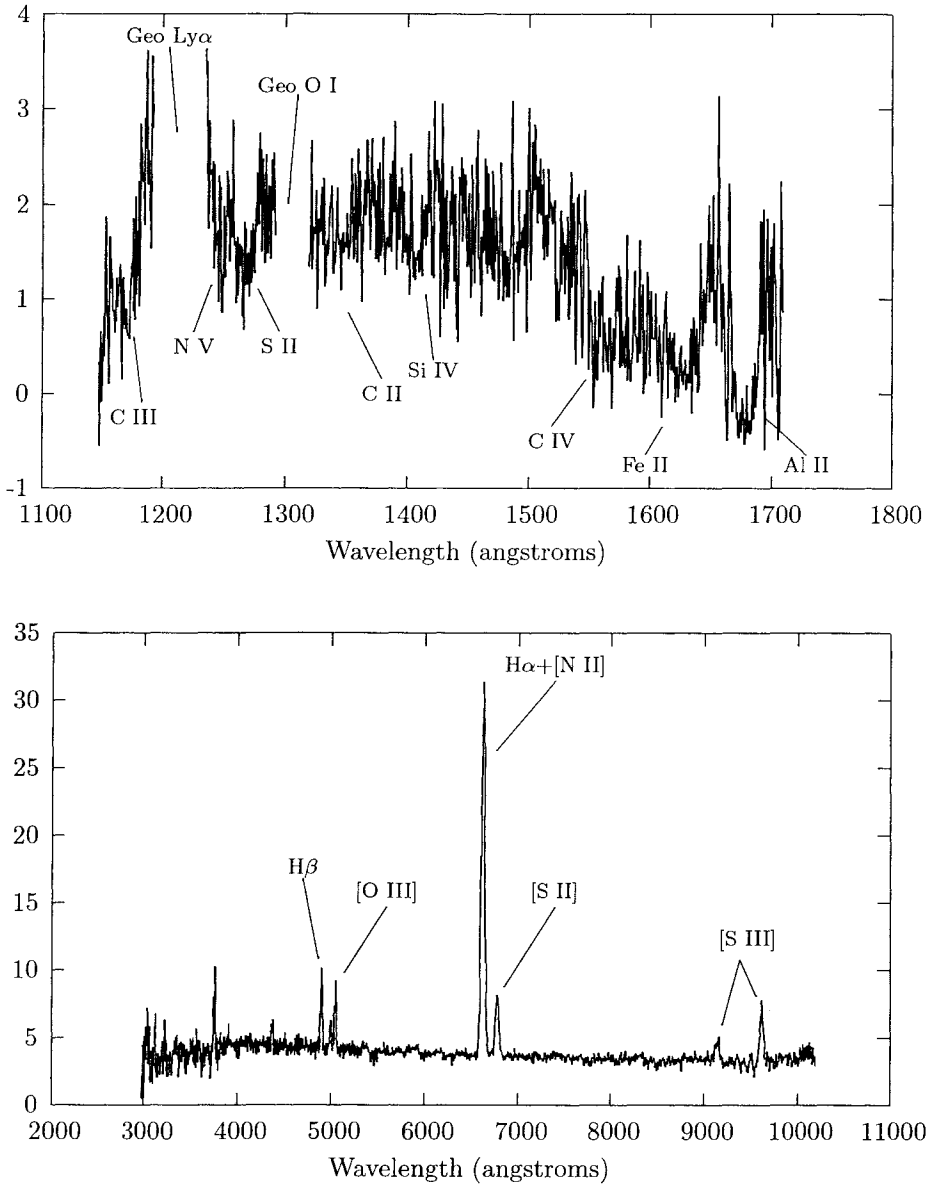

Figure 16 1D spectra of knot 10. The vertical axes are in units of 10^{-16} ergs s^{-1} cm^{-2} $Å^{-1}$ $arcsec^{-2}$

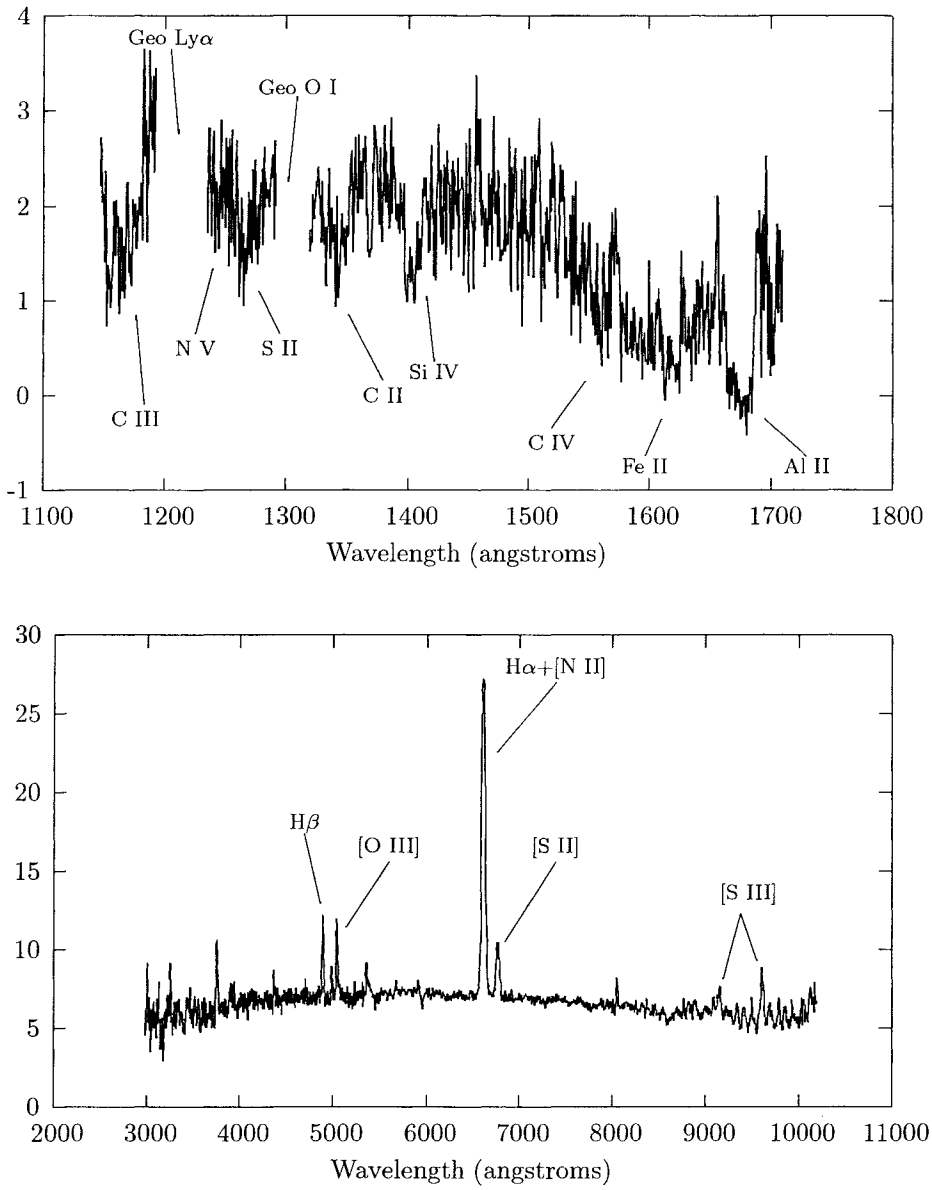

Figure 17 1D spectra of knot 11. The vertical axes are in units of 10^{-16} ergs s^{-1} cm^{-2} $Å^{-1}$ $arcsec^{-2}$

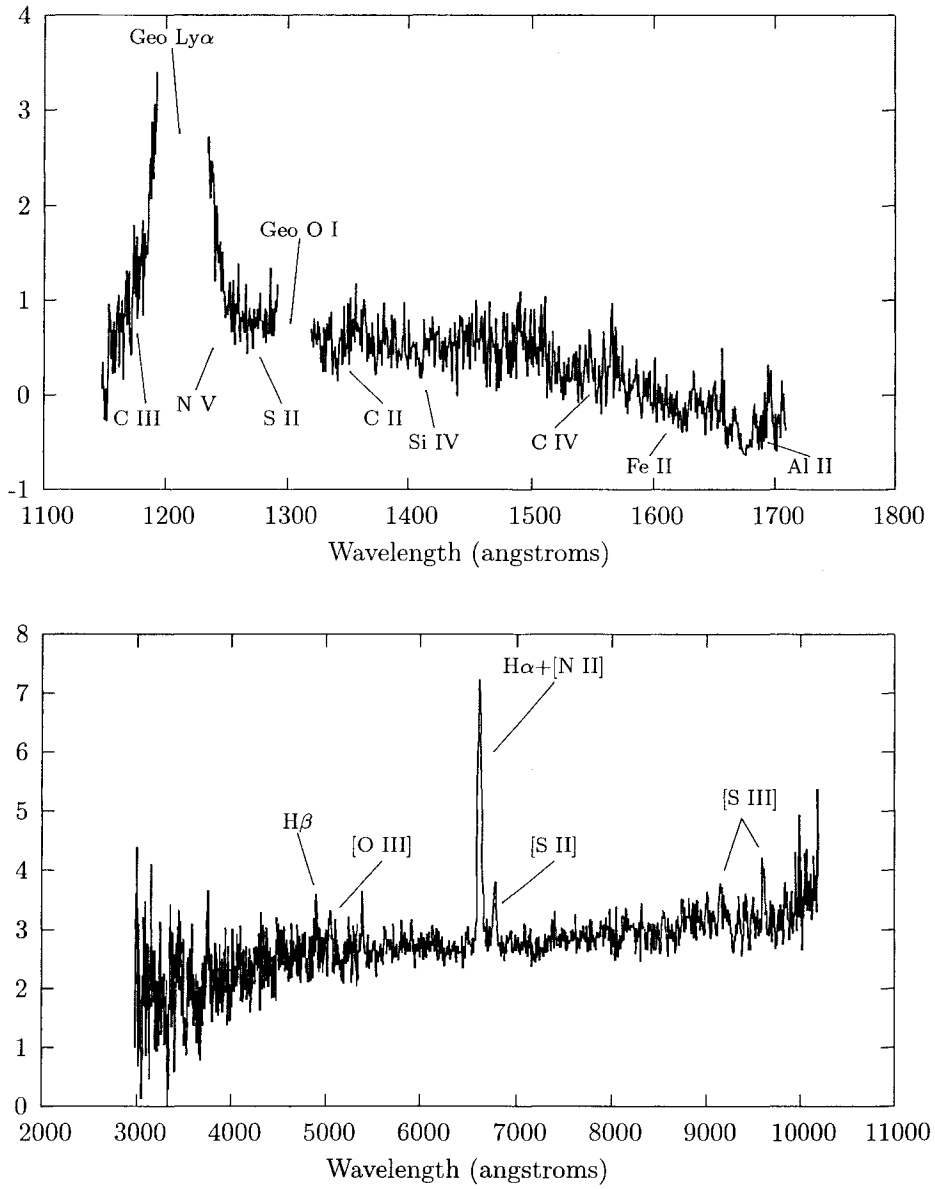

Figure 18 1D spectra of knot 12. The vertical axes are in units of 10^{-16} ergs s^{-1} cm^{-2} $Å^{-1}$ $arcsec^{-2}$

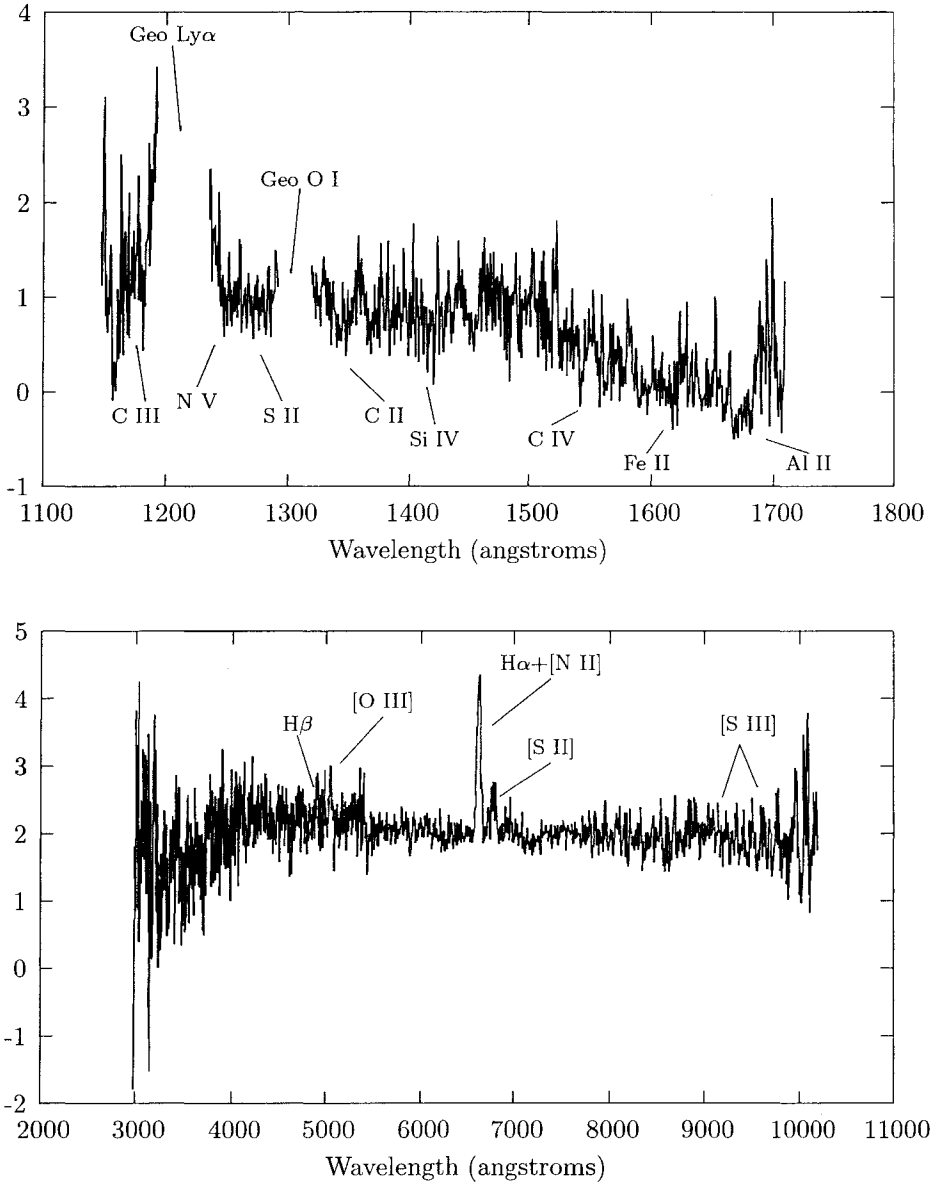

Figure 19 1D spectra of knot 13. The vertical axes are in units of 10^{-16} ergs s^{-1} cm^{-2} $Å^{-1}$ $arcsec^{-2}$

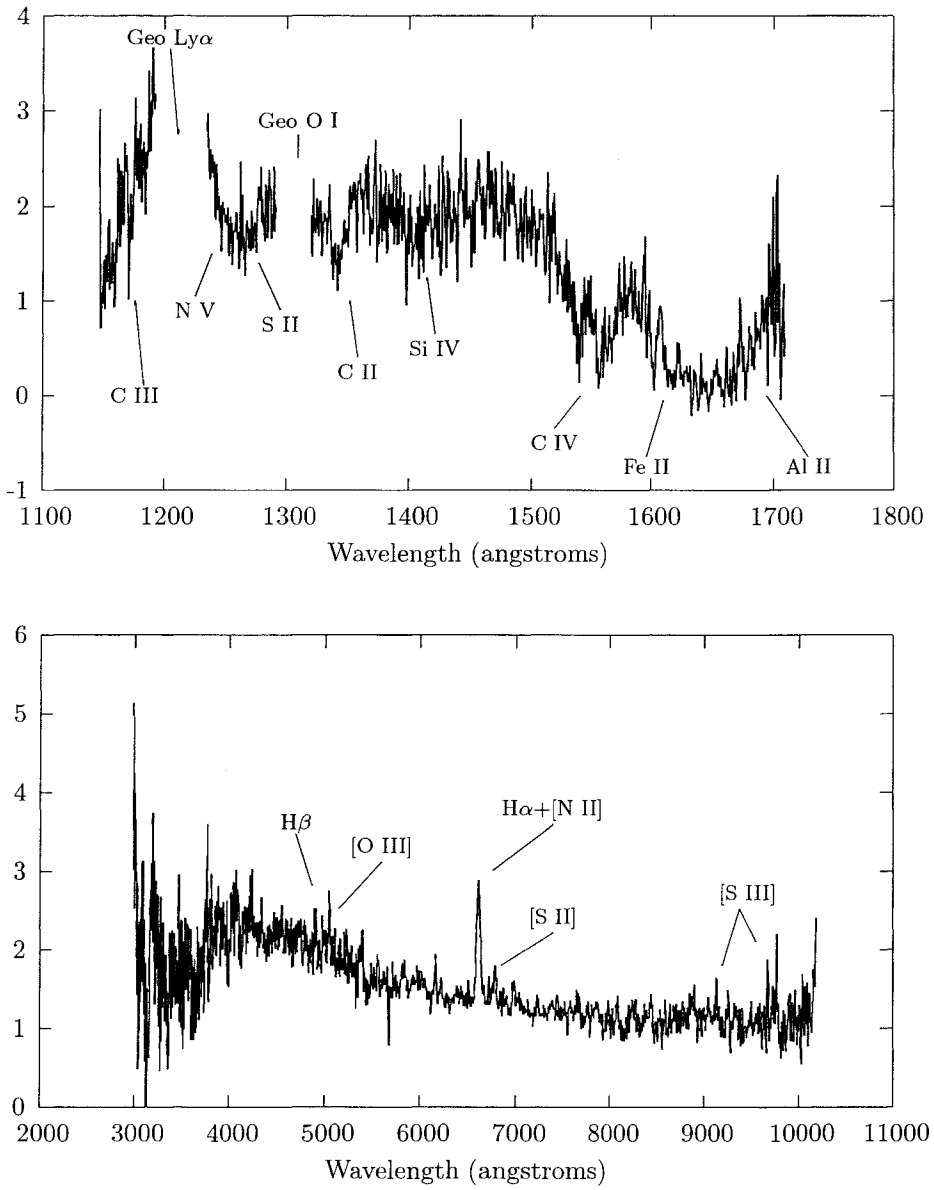

Figure 20 1D spectra of knot 14. The vertical axes are in units of 10^{-16} ergs s^{-1} cm^{-2} $Å^{-1}$ $arcsec^{-2}$

CHAPTER 4

DATA ANALYSIS AND DISCUSSION

Kinematics

A spectral data set provides an observer with much information. We can determine an object's motion by analyzing spectra. NGC 4194 is moving away from us at 2506 km s^{-1} with a redshift of z=0.00836 (de Vaucouleurs *et al.*, 1991). For an assumed inclination of 45°, the galaxy is rotating at ~100 km s^{-1} at a radius of 9″ (Demoulin, 1969).

We have determined the redshift from the spectrum of each of our knots. All of them, except knot 6, have the same redshift (within errors) as the published value for NGC 4194. Parts of the spectrum of knot 6 show a blue shift relative to the other knots. Tables 3-5 list the measured redshifts of the absorption and emission lines. A "- - -" in the table indicates that a redshift measurement could not be made because the line was not present. The Hα+[N II] lines are not individually resolved in our spectra. To measure the redshifts of the Hα lines we assumed a rest wavelength of 6563 Å. The redshifts we calculate for Hα are therefore overestimates. The [S II] $\lambda\lambda$6717, 6731 lines are not individually resolved either. From ground based spectra, see the "Electron Temperature and Density" section, we measure the flux ratio [S II] λ6717 /[S II] λ6731 ~ 1. We assumed that the ratio is the same for all of the knots in our sample and used the average, 6724 Å, as the rest wavelength of the unresolved [S II] $\lambda\lambda$6717, 6731 line to determine the redshifts. Figure 21 shows the average redshift versus position for the 14 knots. The rotation of NGC 4194 seen in Figure 21 is

consistent with the approximate rotation found by Demoulin (1969).

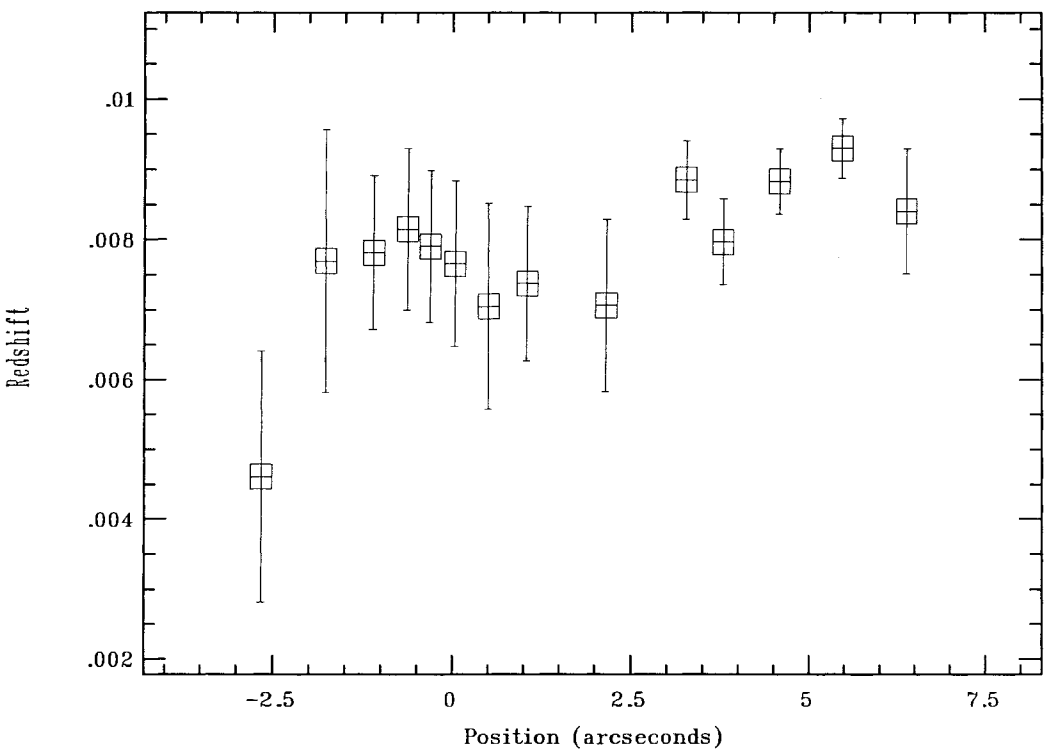

Figure 21 Average redshift vs position along slit

The error bars are 1σ. The errors in the redshift measurements are primarily due to the dispersion. At the distance of NGC 4194, 39.5 Mpc, the width of the slit, 0.5″, corresponds to about 95 pc. The knots in our sample are all much smaller than 95 pc. The typical standard deviation in our redshift measurements is around ± 0.001.

Our spectra are at three different bandpasses. This allows us to study the characteristics of different physical parts of the knots. In the UV, we see absorption features originating in the stellar atmospheres. In the visible, we see emission lines originating in the H II regions. We see Balmer lines in both emission (H II region) and absorption (stellar atmosphere). By studying the redshifts of each of these components, we can ascertain information about the individual motions of different parts of the knots.

In each of the knots, except 6, the difference in redshift between the absorption

Table 3 Redshifts of UV (G140L) Absorption Lines

knot	C III λ1176	N V λ1240	S II λ1260	C II λ1335	Si IV λ1403	Si II λ1527	C IV λ1550	Fe II λ1608	C I λ1657	Al II λ1671
1	0.007	0.006	0.009	0.007	0.005	0.007	0.006	0.007	0.008	0.007
2	0.009	- - -	0.009	0.008	0.005	0.009	0.007	0.006	0.008	0.007
3	- - -	- - -	0.009	0.007	0.005	0.009	0.007	- - -	0.008	0.008
4	- - -	- - -	- - -	0.007	0.005	0.009	0.008	0.006	0.008	0.007
5	- - -	- - -	- - -	- - -	0.004	- - -	0.006	0.007	- - -	0.007
6	- - -	- - -	0.004	0.004	0.004	- - -	0.003	- - -	- - -	0.004
7	- - -	0.006	0.005	0.007	0.004	0.009	0.006	0.006	0.008	0.007
8	0.007	0.006	0.008	0.007	0.004	0.007	0.005	0.007	0.008	0.007
9	- - -	- - -	- - -	- - -	0.005	- - -	0.008	- - -	- - -	0.006
10	- - -	- - -	- - -	- - -	- - -	- - -	- - -	- - -	- - -	- - -
11	- - -	- - -	- - -	- - -	- - -	- - -	- - -	- - -	- - -	- - -
12	- - -	- - -	- - -	- - -	- - -	- - -	- - -	- - -	- - -	- - -
13	- - -	- - -	- - -	- - -	- - -	- - -	- - -	- - -	- - -	- - -
14	- - -	- - -	- - -	- - -	- - -	- - -	- - -	- - -	- - -	- - -

lines and the emission lines is smaller than the error in each measurement. In knot 6, the difference between the redshift of the absorption lines and the single emission line is significant, and suggests that the stellar wind of at least 1 star is moving toward us relative to the H II region. Knot six is the data point at the bottom left of Figure 21.

The emission line in knot 6, Hα, was found to have a redshift of $z_{em} = 0.009$. The UV absorption lines have an average redshift of $<z_{abs}>= 0.004$. The difference in redshift between the emission line and the UV absorption lines is 0.005, therefore the velocity of the stellar winds in knot 6 relative to the associated H II region is about $v \approx 1500$ km s^{-1}. Type B0.5 Ia and Ib, B0 Ia, O9.5 III, O9 V, and O8 I stars have terminal wind velocities in the range 1400 km s^{-1} $< v_{\infty} <$ 1600 km s^{-1} (Kudritzki & Puls, 2000). Prinja & Barlow (1990) define the terminal velocity of a stellar wind as the velocity of out-flowing matter at large distances from the star,

Table 4 Redshifts of Visible (G430L) Emission lines

knot	[O II] λ3727	Hζ λ3889	Hϵ λ3969	Hδ λ4102	Hγ λ4340	[O III] λ4363	Hβ λ4861	[O III] λ4959	[O III] λ5007
1	0.008	0.009	0.009	0.009	0.009	0.009	0.007	0.008	0.008
2	0.009	- - -	0.009	- - -	0.008	- - -	0.008	0.008	0.008
3	0.009	0.009	0.009	0.008	- - -	- - -	0.009	0.008	0.009
4	0.008	0.009	0.009	0.009	0.008	- - -	0.008	0.008	0.008
5	0.009	- - -	- - -	- - -	- - -	- - -	0.009	0.007	0.008
6	- - -	0.006	0.006	0.006	0.006	- - -	- - -	- - -	- - -
7	0.008	0.009	0.008	0.009	- - -	- - -	0.008	0.007	0.007
8	0.008	- - -	0.008	0.009	0.009	0.008	0.008	0.008	0.008
9	0.008	- - -	- - -	- - -	0.009	- - -	0.008	0.008	0.008
10	0.009	- - -	- - -	- - -	0.009	- - -	0.009	0.009	0.009
11	0.008	- - -	- - -	- - -	0.008	- - -	0.008	0.008	0.008
12	0.009	- - -	- - -	- - -	- - -	- - -	0.008	0.009	0.009
13	- - -	- - -	- - -	- - -	- - -	- - -	0.009	- - -	- - -
14	0.009	- - -	- - -	- - -	- - -	- - -	0.009	0.007	0.008

where it is no longer experiencing significant acceleration but is not yet interacting with the interstellar medium. Therefore, the source of the stellar wind in knot 6 is probably massive O and B stars.

The EW(Hα) indicates that the age of knot 6 is $8.5 - 10.5$ Myr (see the "Ages of the Knots" section). A knot with this age could still contain O and B stars. All of the stars in a knot probably do not form at precisely the same time, so some of the O and B stars could be younger than the EW(Hα) suggests.

Knot 6 shows one emission line, indicating that there is very little gas surrounding the stars. The UV absorption lines in knot 6 are blue shifted relative to the H II region, indicating the presence of stellar winds. For knot 6 then, we are looking at the fast moving stellar wind. This wind has blown out most of the gas in the nebulae as is evidenced by the lack of Balmer emission. The Balmer lines are in absorption except for Hα . The lack of gas and the presence of blue shifted stellar winds lead us to

Table 5 Redshifts of Visible (G750L) Emission lines

knot	Hα^a	[S II]^b	[S III]	[S III]
	λ6563	λ6724	λ9069	λ9531
1	0.009	0.006	0.008	0.008
2	0.009	0.007	- - -	- - -
3	0.009	0.007	- - -	- - -
4	0.009	0.007	- - -	- - -
5	0.009	0.007	- - -	- - -
6	0.009	- - -	- - -	- - -
7	0.008	0.006	- - -	- - -
8	0.008	0.007	0.008	0.008
9	0.009	0.007	0.009	0.009
10	0.010	0.008	0.009	0.009
11	0.009	0.007	- - -	0.008
12	0.009	- - -	- - -	- - -
13	0.010	- - -	- - -	- - -
14	0.009	- - -	- - -	- - -

[a] blended with [N II] $\lambda\lambda$6548, 6583

[b] unresolved [S II]$\lambda\lambda$6717, 6731

believe that knot 6 is a Bubble. A Bubble is a volume of space that has been emptied of its gas by the outward flow of the stellar winds of massive stars.

Emission Line Strengths

To measure the flux in an emission line one must account for the fact that the dispersion axis is not uniformly illuminated. Only emission lines need this correction. The calibrations in the CALSTIS pipeline assume a uniform point source illumination. To make this correction, one needs to sum the pixels in the emission line and multiply by the CONT2EML value from the image header. The CONT2EML term is simply the slit width in angstroms. When making this dispersion correction it is important to ensure that the dispersion is not already accounted for when summing the pixels

in the emission line. Before the correction, our 1D spectra have units of 10^{-16} ergs s^{-1} cm^{-2} $Å^{-1}$ $arcsec^{-2}$. After the CONT2EML dispersion correction, the units for the emission line fluxes are 10^{-16} ergs s^{-1} cm^{-2} $arcsec^{-2}$.

After one does the CONT2EML correction to the emission lines, a correction for stellar absorption must be applied to the Balmer lines. The Balmer lines are seen in absorption in the atmospheres of stars, so there is underlying absorption in the nebular emission lines since our spectra are a combination of emission/absorption from stars and H II regions. To correct for this, 2 Å of continuum flux at each hydrogen line was added to the flux of the line (McCall, Rybski, & Shields, 1985).

The fluxes of several emission lines have been measured, including emission lines originating in [O II] λ3727 , [O III] λ4959 , [O III] λ5007 , and H. The equivalent widths of several absorption lines have also been measured. The most prominent absorption features are in the ultraviolet and include C IV λ1550 and Si IV λ1403 . Table 6 lists our measured fluxes and Table 7 lists our measured equivalent widths. The negative sign in front of an equivalent width indicates the line is in emission.

Reddening Correction

To correct the measured line fluxes for reddening we used the Calzetti, Kinney, & Storchi-Bergmann (1994) reddening law, $Q(x) = -2.156 + 1.509x - 0.198x^2 + 0.011x^3$, where $x = \lambda^{-1}(\mu m^{-1})$. This effective extinction law was derived from star forming galaxies like ours and is greyer than the standard Galactic extinction law. Grey means that the extinction coefficient is independent of wavelength.

The measured fluxes were corrected by considering, $I_\lambda = I^o_\lambda e^{-\tau_\lambda}$, where I_λ is the observed intensity, I^o_λ is the unreddened source intensity and τ_λ is the optical depth. The optical depth is expressed as $\delta\tau_\lambda = -\kappa_\lambda \rho \delta s$, where κ_λ is the opacity, ρ is the density and s is the path length along a line of sight. For a particular, but unknown,

Table 6 Measured Flux

knot	[O II][a] λ3727	Hβ[a] λ4861	[O III][a] λ4959	[O III][a] λ5007	Hα+[N II][a] λ6563
1	2794	964	985	2855	11339
2	2738	1349	445	1453	11094
3	2903	1138	591	1057	10208
4	1543	778	306	798	5918
5	905	304	133	354	2321
6	- - -	- - -	- - -	- - -	721
7	1002	7583	724	2159	5023
8	1903	2467	1014	3236	28943
9	794	630	260	707	7231
10	1137	1280	325	1119	12463
11	932	1046	328	1207	9985
12	338	170	96	251	2023
13	- - -	98	- - -	- - -	1202
14	244	104	81	163	720

[a] flux in units of 10^{-16} erg s^{-1} cm^{-2} $arcsec^{-2}$

path length, the optical depth can be written as cf(λ), where c depends on the amount of absorbing material in the line-of-sight to the observed star and f(λ) is a function of wavelength that is assumed to be the same for all stars (Osterbrock, 1989). We replaced f(λ) with the Calzetti, Kinney, & Storchi-Bergmann (1994) reddening law Q(x).

To determine c, and thus the amount of extinction, we considered an emission line ratio that only weakly depends on temperature,

$$\frac{\mathrm{H}\alpha}{\mathrm{H}\beta} = \frac{\mathrm{H}\alpha^o}{\mathrm{H}\beta^o} 10^{c[Q(\lambda 4861) - Q(\lambda 6563)]}$$

Using recombination theory, case B, one can determine the theoretical unreddened $\mathrm{H}\alpha^o/\mathrm{H}\beta^o = 2.87$ (Osterbrock, 1989). We then measured the Hα /Hβ ratio from the spectra and solved for the constant c for each knot. The value determined for c was used to correct the rest of the emission lines. We were unable to de-blend the [N II]

Table 7 Measured Equivalent Width

knot	Si IV[a] λ1403	C IV[a] λ1550	Hβ[a] λ4861	Hα+[N II][a] λ6563
1	5.6	9.5	-6.1	-86.6
2	6.4	8.1	-15.8	-174
3	6.6	9.9	-10.8	-121
4	6.9	13.5	-13.9	-133
5	3.4	11.1	-10.9	-90.1
6	6.4	13.3	- - -	-24.9
7	4.9	17.7	-9.6	-91.8
8	6.2	12.1	-13.0	-175
9	4.1	12.6	-21.8	-220
10	- - -	- - -	-32.5	-337
11	- - -	- - -	-16.8	-142
12	- - -	- - -	-8.2	-73.6
13	- - -	- - -	-6.1	-63.2
14	- - -	- - -	-7.1	-55.6

[a] equivalent width in Å

$\lambda\lambda$6548, 6583 lines from the Hα line so the entire Hα+[N II] emission was used, over estimating the value of c.

The color excess, E(B−V), can be determined in terms of the Calzetti reddening law by noting that the excess is just

$$\mathrm{E(B-V)} = (\mathrm{B-V})_{observed} - (\mathrm{B-V})_{unreddened}$$

and that

$$(\mathrm{B-V}) = 2.5 \log\left(\frac{\mathrm{I}_V}{\mathrm{I}_B}\right)$$

where

$$\left(\frac{\mathrm{I}_V}{\mathrm{I}_B}\right)_{observed} = \left(\frac{\mathrm{I}_V}{\mathrm{I}_B}\right) 10^{c[Q(B)-Q(V)]}$$

We determine the average E(B−V)=1.1 mag. for 13 knots (see Table 8). This extinction was determined using the entire Hα+[N II] emission. To get a better esti-

mate of the extinction we need to determine the contribution of the [N II] $\lambda\lambda$6548, 6583 emission lines. The measured [O III]λ5007/Hβ ratio in our spectra is consistent with a [N II] $\lambda\lambda$6548, 6583 contamination of approximately 40% in the unresolved Hα+[N II] emission line (Osterbrock 1989). Ground based spectra of NGC 4194 show mostly resolved Hα+[N II] emission lines. See the "Electron Temperature and Density" section for a description of the ground based spectra. We measured the entire Hα+[N II] flux in the ground based spectra. We then measured the [N II] λ6583 flux in the same spectra. For all the ground based spectra we find the [N II] λ6583/(Hα+[N II])$\sim$ 0.3. We know from the ratio of the transition probabilities that the flux ratio of [N II] λ6583/[N II] λ6548 is 3 so the contamination in the entire Hα+[N II] complex due to [N II] $\lambda\lambda$6548, 6583 is roughly 40%. If one assumes a contamination of [N II] $\lambda\lambda$6548, 6583 =40% the average E(B$-$V)=0.7 mag.

Table 8 Extinction

Knot	E(B-V)	E(B-V)[a] (min)
1	1.3	0.9
2	1.0	0.5
3	1.1	0.6
4	0.9	0.4
5	0.9	0.4
6	- - -	- - -
7	1.0	0.6
8	1.3	0.8
9	1.3	0.8
10	1.2	0.7
11	1.1	0.7
12	1.3	0.9
13	1.4	0.9
14	0.8	0.4
Average	1.1	0.7

[a] assuming [N II] contribution of 40%

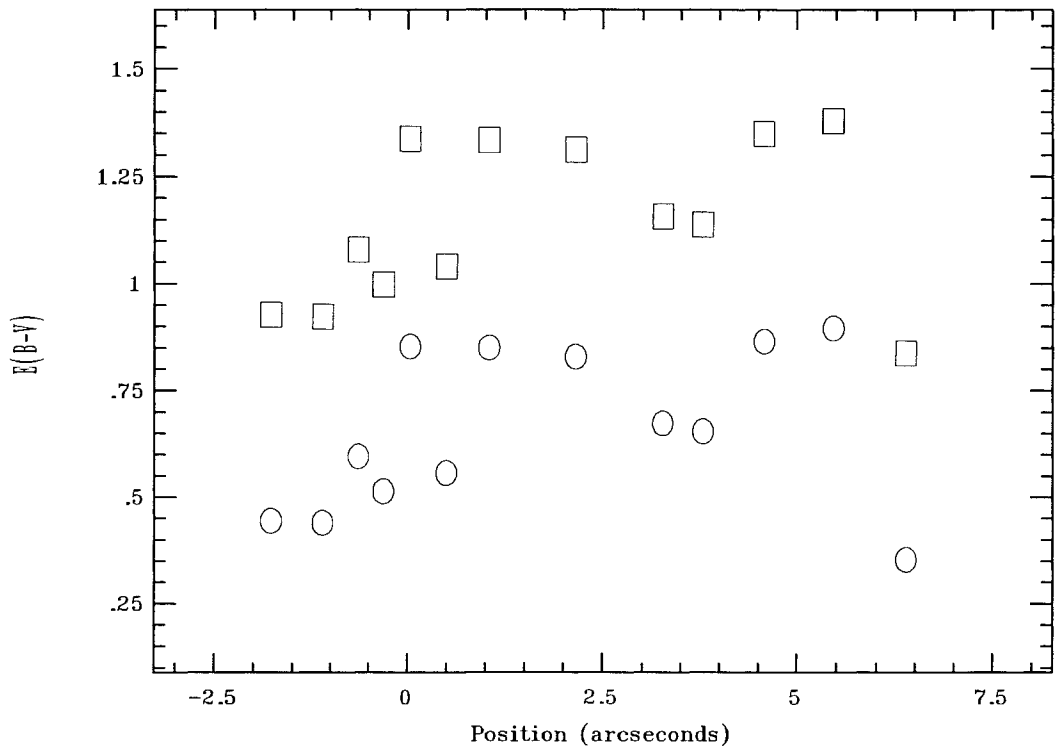

Figure 22 E(B-V) vs Position

Weistrop *et al.* (2004) found that the most likely extinction of a large sample of star forming knots in NGC 4194, determined from photometry and model comparison, was E(B−V)=0.3 mag. Previous results have shown that there is a difference of a factor of about 2 in the reddening determined from emission lines and continuum observations. This may be due to the fact that the H II regions surrounding the hot stars in the nebula are dustier than the regions containing the cooler stars contributing to the continuum (eg. Calzetti, Kinney, & Storchi-Bergmann (1994)). If we correct the average minimum reddening for this difference, we find the knots have E(B−V)=0.4 mag. The reddening we have determined here is consistent with Weistrop *et al.* (2004). The extinction and minimum extinction are listed in Table 8. There is no reported reddening for knot 6 because Hβ is in absorption.

Figure 22 is a plot of E(B−V) as a function of position along the slit in angular

coordinates. A position zero marks the center of the slit. The boxes are E(B−V)and circles are minimum E(B−V). From this plot it can be inferred that the extinction increases from $-2.5''$ from the slit center to 0 and is roughly constant until it decreases again around $6''$ from slit center.

Metallicity

The metal abundances for the knots have been determined with several calibrations using the equivalent widths of UV absorption lines and the oxygen emission line ratios. The C IV λ1550 and Si IV λ1403 equivalent widths were used to determine log(O/H)+12 using the calibrations in Storchi-Bergmann, Calzetti, & Kinney (1994),

$$\mathrm{EW(C\ IV\ }\lambda1550) = (10.6 \pm 1.3) \times (\log(\mathrm{O/H}) + 12) - (83.4 \pm 10.8)$$

$$\mathrm{EW(Si\ IV\ }\lambda1403) = (6.6 \pm 1.0) \times (\log(\mathrm{O/H}) + 12) - (50.1 \pm 8.5)$$

Following the prescription of Kewley *et al.* (2002) we used the emission line ratio of R_{23}=([O II] λ3727 + [O III]$\lambda\lambda$4959, 5007)/Hβ to calculate log(O/H)+12 using the calibration of Zaritsky, Kennicutt, & Huchra (1994),

$$\log(\mathrm{O/H}) + 12 = 9.265 - 0.33x - 0.202x^2 - 0.207x^3 - 0.333x^4$$

and the high metallicity upper branch calibration of McGaugh (1991) as parameterized by Kobulnicky, Kennicutt, & Pizagno (1999),

$$\log(\mathrm{O/H}) + 12 = 12 - 2.939 - 0.2x - 0.237x^2 - 0.305x^3 - 0.0283x^4$$

$$-y(0.0047 - 0.0221x - 0.102x^2 - 0.0817x^3 - 0.00717x^4)$$

where x=log(R_{23}), and y=log([O III] $\lambda\lambda$4959, 5007)/[O II] λ3727).

An S_{23}=([S II]$\lambda\lambda$6717, 6731+[S III]$\lambda\lambda$9069, 9532)/Hβ calibration was not used to derive log(O/H)+12. Kewley *et al.* (2002) state that S_{23} calibrations do not reliably estimate abundances for any metallicity range.

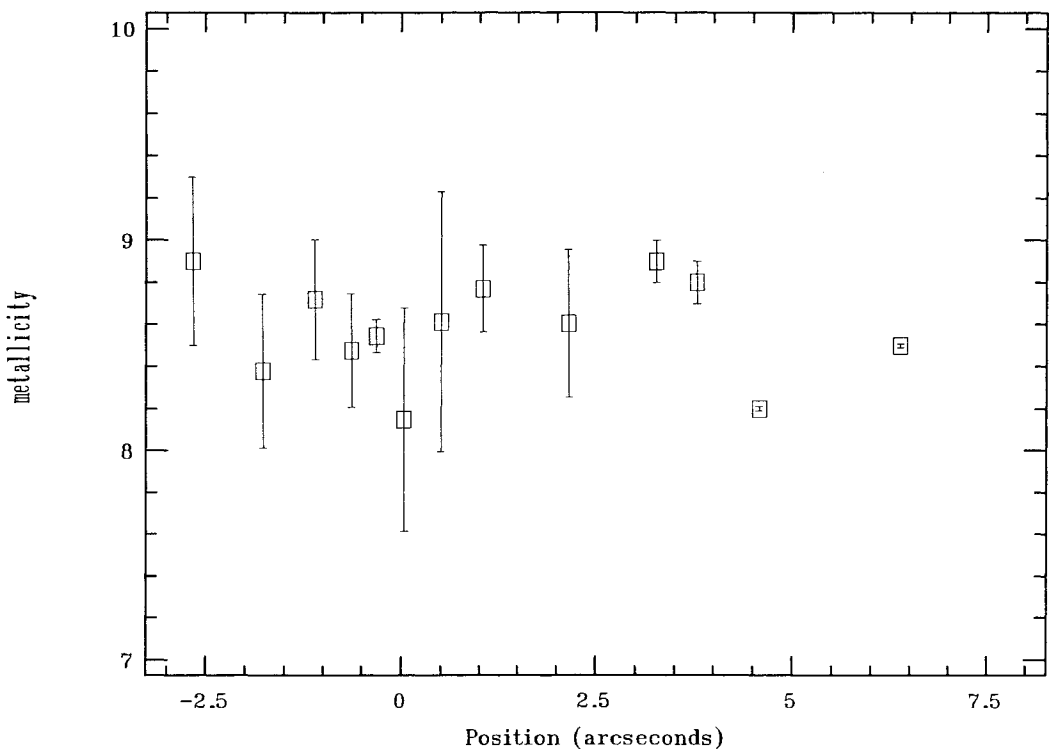

Figure 23 Metallicity vs Position

The abundances derived from each calibration and the average abundance can be seen in Table 9. A "- - -" in Table 9 means that at least one of the diagnostic lines was not present, so a metal abundance calculation was not possible. The average abundances calculated range from 8.1±0.5 to 8.9±0.1. The abundances calculated are in good agreement and are approximately solar (Z=8.92). This further confirms the assumption of solar abundance in the model analysis of Weistrop *et al.* (2004). Our findings are also consistent with Storchi-Bergmann, Calzetti, & Kinney (1994) who found log(O/H)+12 = 8.81 and Heckman *et al.* (1998) who report log(O/H)+12>8.6 for NGC 4194.

Figure 23 is a plot of the average metallicity against position along the slit in angular coordinates. Zero marks the center of the slit. The metallicity in the figure is the average of the metallicities determined by all four calibrations. The plots for

the individual calibrations are similar so are not shown. It can be seen from Figure 23 that there is no obvious dependence of metallicity on position.

Table 9 Calculated Abundances

Knot	$Z_{C\ IV}$[a]	$Z_{Si\ IV}$[a]	Z_{Z94}[b]	Z_{M91}[c]	average
1	8.8	8.4	7.6	7.8	8.1±0.5
2	8.6	8.6	8.6	8.4	8.5±0.1
3	8.8	8.6	8.3	8.2	8.5±0.3
4	9.1	8.6	8.6	8.5	8.7±0.3
5	8.9	8.1	8.3	8.2	8.4±0.4
6	9.1	8.6	- - -	- - -	8.9±0.4
7	9.6	8.3	8.3	8.3	8.6±0.6
8	9.0	8.5	8.8	8.7	8.8±0.2
9	9.1	8.2	8.6	8.5	8.6±0.3
10	- - -	- - -	8.9	8.8	8.9±0.1
11	- - -	- - -	8.9	8.7	8.8±0.1
12	- - -	- - -	8.2	8.2	8.2±0.01
13	- - -	- - -	- - -	- - -	- - -
14	- - -	- - -	8.5	8.4	8.5±0.01

[a] log(O/H)+12, Storchi-Bergmann, Calzetti, & Kinney (1994)
[b] log(O/H)+12, Zaritsky, Kennicutt, & Huchra (1994)
[c] log(O/H)+12, Kobulnicky, Kennicutt, & Pizagno (1999)

Star Formation Rate

At what rate are the knots forming stars? We can determine the Star Formation Rate (SFR) from measurements of two emission lines. Hα is a recombination line, so it is a direct tracer of the ultraviolet emission. From the Hα luminosity we can estimate the number of ionizing photons emitted by the stars and absorbed in the surrounding H II region. For an assumed luminosity function or IMF, the Hα luminosity gives the number of stars in each spectral type being formed. Since main sequence stars that have strong UV emission have very short lifetimes, their present number divided

by their lifetimes is the current SFR. Hα is redshifted out of the visible wavelength region beyond z$\sim$ 0.5, so the calibration of a line in the blue for the determination of SFRs was needed. The forbidden [O II] λ3727 line is also a good SFR tracer. The first ionization potential for oxygen is 13.6 eV, so the presence of O II also traces the UV radiation field.

The SFR determined with Hα measurements is sensitive to uncertainties in the extinction and in the form of the assumed IMF. The assumption that all of the ionizing photons are absorbed is not completely correct. The escape fraction of ionizing radiation from individual H II regions in nearby galaxies has been observed to be between 15-50% (e.g. Kennicutt (1998), and references therein).

The SFR determined from [O II] λ3727 is less precise than the SFR determined from an Hα measurement. The [O II] λ3727 SFR is calibrated empirically through Hα (Kennicutt, 1998). The strength of [O II] λ3727 is not directly coupled to the number of ionizing photons. The presence of O II indicates that there are ionizing photons. The number of [O II] λ3727 photons also depends on the collision rate, which depends on, among other things, the density. It requires a 3.3 eV collision to produce an [O II] λ3727 photon. It requires stars of temperatures around 4×10^4 K to provide enough thermal energy for such collisions. The [O II] λ3727 line is bluer than Hα so is more sensitive to extinction. The excitation of [O II] λ3727 is sensitive to the abundance of oxygen and ionization state of the gas. The [O II] λ3727/Hα ratio in individual galaxies can vary between 0.5-1.0 dex (Kennicutt, 1998).

To determine the Hα+[N II] luminosity, L(Hα+[N II]), and [O II] λ3727 luminosity, L([O II]λ3727), the reddening corrected fluxes were converted to luminosities by multiplying by $4\pi R^2$, where R is the distance to NGC 4194. This was done as follows. The relative flux of each of the two lines was multiplied by the absolute flux of Hβ . The flux units are ergs s^{-1} cm^{-2} $arcsec^{-2}$. The angular dependence was removed by

multiplying by the number of arcseconds in the spatial direction and the number of arcseconds in the dispersion direction. The number of arcseconds in the spatial direction was determined by the product of the number of pixels in the aperture defining the knot and the number of arcseconds per pixel. The number of arcseconds in the dispersion direction was determined by the product of the width of the line at the continuum in pixels and the number of arcseconds per pixel. For the CCD detectors there are 0.0507 arcseconds per pixel. We adopt a distance of 39.5 Mpc (Weistrop *et al.*, 2004). The fluxes used to determine the luminosities were average fluxes, (see the "One Dimensional Extraction" section). To determine the total luminosity of a knot we multiplied each by the number of pixels in the aperture defining the knot. The luminosities are in units of erg s^{-1}. Table 10 lists the L(Hα+[N II]) , L([O II] λ3727) , L(Hβ) , SFR from Hα+[N II] , SFR from Hα , SFR from [O II] λ3727 and the size of each of the knots. See the "Sizes of the Knots" section for details on the size determinations.

We could not resolve the [N II] $\lambda\lambda$6548, 6583 lines and the Hα line, so the star formation rate was calculated from the Hα+[N II] and [O II] λ3727 luminosities. The combined L(Hα+[N II]) of all the knots in our sample yield a SFR of $\sim$77 $M_\odot$ yr^{-1}using SFR($M_\odot$ yr^{-1})= 7.9×10^{-42}L(Hα) (ergs s^{-1}) assuming a standard Salpeter IMF (Kennicutt, 1998). The true Hα flux is less than the combined Hα+[N II] flux we measured, so the SFR may be as much as 40% smaller than reported if our previous assumption about the [N II] contribution is made. The corrected Hα flux would result in a total SFR of $\sim$46 $M_\odot$ yr^{-1}. The combined [O II] λ3727 luminosity of all the knots in our sample yield a SFR of approximately 141 $M_\odot$ yr^{-1}using SFR($M_\odot$ yr^{-1})= $(1.4 \pm 0.4) \times 10^{-41}$L([O II] λ3727) (ergs s^{-1}) (Kennicutt, 1998). The SFR determined from L([O II] λ3727) is considerably higher than the other two determinations. The uncertainties in the equation indicate a range between blue emission line galaxies

Table 10 Luminosities, SFRs and Sizes

Knot	L[a] (Hα+[N II])	L[a] ([O II])	L[a] (Hβ)	SFR[b] (Hα+[N II])	SFR[b,d] (Hα)	SFR[b,c] ([O II])	Size (pc)
1	5.0	14	0.83	4.0	2.4	20±5.6	58
2	1.1	1.6	0.23	0.88	0.53	2.2± 0.6	38
3	1.6	3.5	0.32	1.3	0.75	4.9±1.4	42
4	4.6	5.7	0.95	3.6	2.2	8.0±2.2	61
5	3.6	6.2	0.69	2.8	1.7	8.7±2.5	54
6	- - -	- - -	- - -	- - -	- - -	- - -	- - -
7	1.4	1.6	0.33	1.1	0.64	2.2± 0.6	43
8	28	17	4.9	22	13	24± 7.0	105
9	33	36	7.2	26	16	50± 14	119
10	4.7	2.5	0.88	3.7	2.2	3.5± 1.0	59
11	9.7	5.0	1.7	7.7	4.6	7.0± 2.0	73
12	2.6	4.4	0.45	2.0	1.2	6.2±1.8	47
13	0.58	- - -	0.09	0.46	0.28	- - -	28
14	2.2	3.7	0.63	1.8	1.1	5.2± 1.5	53
Total	97	101	19	77	46	141±17	- - -

[a] Total Knot Luminosity is in units of 10^{41} ergs s^{-1}

[b] Star Formation Rate is in units of $M_\odot$ yr^{-1}

[c] error does not include error in L([O II])

[d] assuming 40% [N II] contribution

(lower limit) and samples of more luminous spiral galaxies (upper limit) (Kennicutt, 1998). Weistrop *et al.* (2004) found the SFR of 25 knots younger than 20 Myr in NGC 4194 to be 6 $M_\odot$ $yr^{-1}$and determined that the total SFR could be as high as around 30 $M_\odot$ yr^{-1}. The total SFR determined by Weistrop *et al.* (2004) was calculated from the total background UV flux in the center of NGC 4194. The agreement of our total SFR with Weistrop *et al.* (2004) suggests that the UV background flux 'escaped' from the knots. The SFR we find from our corrected Hα luminosity is consistent with Storchi-Bergmann, Calzetti, & Kinney (1994), who find a total SFR of around 38 $M_\odot$ $yr^{-1}$for NGC 4194. For comparison, the SFR of the entire Milky Way is on the order of 1 $M_\odot$ yr^{-1}.

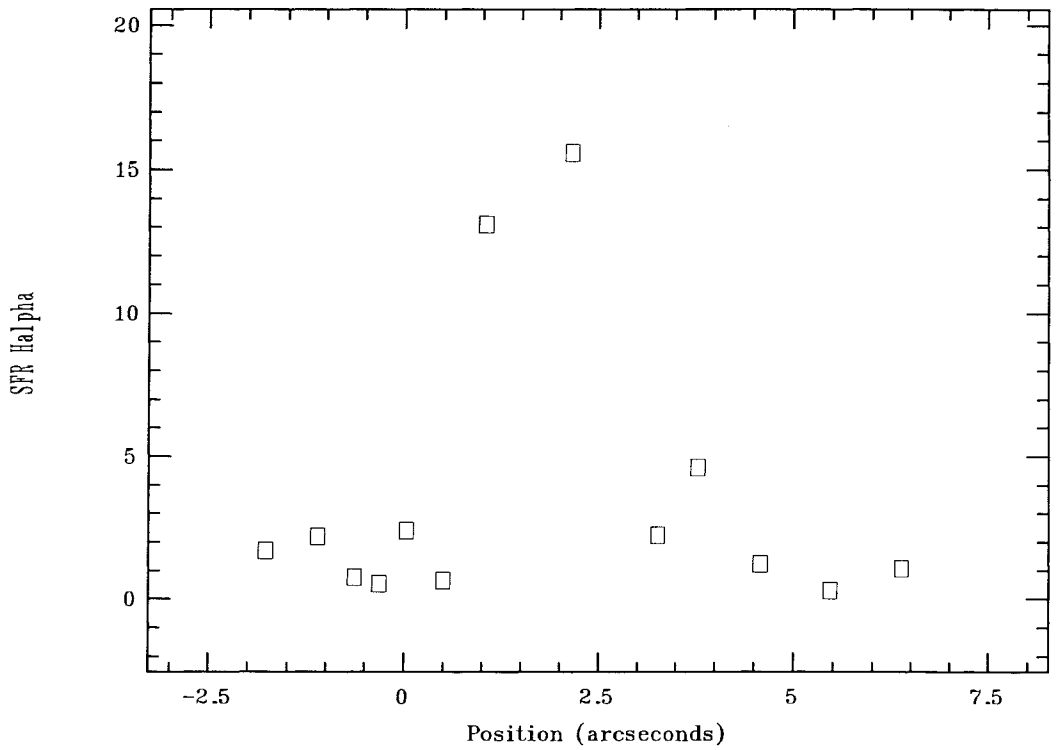

Figure 24 SFR vs Position

Figure 24 is a plot of the SFR as determined from our corrected Hα luminosity against position along the slit. The shape of the SFR distribution as determined by Hα+[N II] and [O II] λ3727 are similar to Figure 24 so are not shown. From this plot it can be seen that the SFR is the greatest near the center of NGC 4194.

Figure 25 is a plot of the SFR as determined from the corrected Hα luminosity versus the average log(O/H)+12. The error bar represents the average error in abundance. There does not appear to be a correlation between the SFR and abundance.

Electron Temperature and Density

That the stars in the knots are surrounded by gas as is evidenced by the Balmer emission lines, for example. By measuring the strengths of certain emission lines

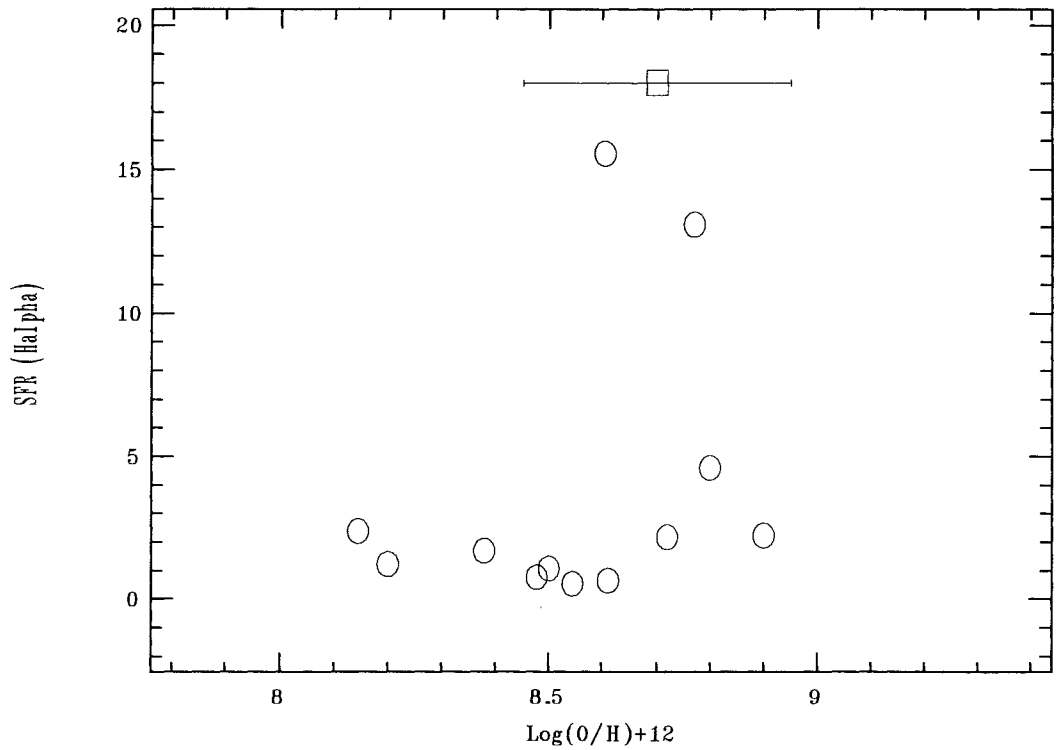

Figure 25 SFR vs Abundance

emitted by the gas, we can determine the temperature and density of the electrons in the gas.

The electron temperature can be determined by measuring emission line ratios that depend strongly on temperature. The energy level structure of O III is such that emission lines from two different upper levels occur with considerably different excitation energies. The electrons are collisionally excited from the ground ^{3}P level. The [O III] λ4363 line is a downward radiative transition from the ^{1}S level. The [O III] λ4959 and [O III] λ5007 lines both originate in the ^{1}D level. The relative populations of the upper levels depends very strongly on temperature because these are collisionally excited lines. The measured ratio ([O III] λ4959 + [O III] λ5007)/[O III] λ4363 can be used to determine the electron temperature. The lines are all close in wavelength, so the effects of extinction on the ratio is negligible.

The ratio of the emission line fluxes is equal to the ratio of the emission coefficients. The emission coefficients depend on the radiative transition rates, the collisional transition rates and the electron temperature and density. From Osterbrock (1989), the ratio of the oxygen emission coefficients can be written as,

$$\frac{j_{\lambda 4959} + j_{\lambda 5007}}{j_{\lambda 4363}} = \frac{7.73\, e^{(3.29\times 10^4)/T}}{1 + 4.5 \times 10^{-4}(N_e/T^{1/2})}$$

where j_λ is the emission coefficient for the species at wavelength λ, T is the electron temperature and N_e is the electron density.

The electron density can be determined by observing collisional de-excitation effects. The excitation rates of two collisionally excited lines of the same ion with nearly the same excitation energies depends only on the ratio of the collision strengths to those levels. If the two levels have different collisional de-excitation rates, the relative populations depend on the density (Osterbrock, 1989). An example of such a set of emission lines in the visible spectrum is the [S II] λ6717 and [S II] λ6731 pair.

The temperatures and densities were determined from ground based spectra of the central regions of NGC 4194. The spectra from three different slit position angles were recorded at KPNO from the 10th to the 12th of June 1999. The slit positions were chosen to maximize the coverage of star forming regions. The ground based spectra have better spectral resolution but poorer spatial resolution than our STIS spectra. The star forming regions from which the temperatures and densities are derived are not resolved and are not the same as those from our STIS data. Some of the star forming regions may coincide, but not all. However, the ground based spectra are from the same central region of NGC 4194 as the STIS spectra so we assume the physical properties are similar.

The IRAF task TEMDEN in the NEBULAR package was used to carry out the calculations (Shaw & Dufour, 1995). The TEMDEN task calculates either an N_e or temperature for an ionized nebular gas for an assumed temperature or N_e. One must

provide an appropriate diagnostic line ratio.

The dependence on N_e is stronger than on T. This means that a small change in T will have a small effect on the calculation of N_e. However, a small change in N_e will have a larger effect on the calculation of T. Therefore, we first calculated the electron density with an assumed temperature of 10,000 K. The temperatures were then calculated with the previously determined electron densities. The electron densities were then calculated again assuming the new temperature. This process was iterated until the values for the densities and temperatures converged. It only took three iterations for the values to converge in each case. The position angle of the slit, [O III] and [S II] line ratios, electron temperature, and the electron density are shown in Table 11.

Table 11 Electron Temperatures and Densities

Position Angle	[O III] ratio	[S II] ratio	Temperature (K)	Density (cm^{-3})
pa131	122.1	1.04	11900	545
pa164	194.7	1.04	10200	517
pa68	196.5	1.01	10200	586
pa68b	135.7	1.07	11500	472
average			11000	530

Sizes of the Knots

The sizes of the knots were determined from L(Hβ). The Hβ line was used because it is not contaminated by [N II] $\lambda\lambda 6548, 6583$ like the Hα line. The sizes we determine for the knots are the sizes of the H II regions surrounding the stars, and not the size of the 'cluster' of stars. To calculate the size of a knot one can write the L(Hβ) as

$$L(H\beta) = \frac{4\pi}{3} r^3 \epsilon N_e N_p \alpha_{H\beta}^{eff} h\nu_{H\beta}$$

where ϵ is a filling factor, r is the radius of the knot, N_e is electron density, N_p is proton density, h is Planck's constant, $\nu_{H\beta}$ is the frequency of a Hβ photon, $\alpha_{H\beta}^{eff}$ is the effective recombination coefficient for Hβ, and L(Hβ) is the luminosity of Hβ. L(Hβ) was calculated in the same way as L(Hα) and is described in the "Star Formation Rate" section. Solving for r gives the size of the H II region. To make this calculation, one must make some assumption about the clumpiness of the gas in the knot. We assumed a clumpy distribution, a filling factor of 0.1, and show the sizes in Table 10. Applying a filling factor of 1, a uniform gas distribution, will result in a smaller knot size. The sizes reported in the table are therefore upper limits. A filling factor of 1 will decrease the size by a factor of $10^{1/3} \approx 2.15$.

We determined our choice of filling factor, $\epsilon = 0.1$ by using the Starburst99 (SB99) model (Leitherer *et al.*, 1999) to estimate the value of ϵ. According to Starburst99, a 6 Myr old knot with solar abundances has an EW(H$\beta)_{SB99}$ of 17.66 Å. The subscript "SB99" will be used to refer to values taken from the starburst99 model. The L(H$\beta)_{SB99}$ of the 6 Myr old knot is 6.97×10^{37} erg s^{-1} Å^{-1}. The L(H$\beta)_{SB99}$, in erg s^{-1} can be determined by multiplying the L(H$\beta)_{SB99}$ (erg s^{-1} Å^{-1}) by EW(H$\beta)_{SB99}$ (Å). This assumes that the model continuum in the region of Hβ is flat. In fact the continuum in this region is not flat and changes by a factor ~ 3 in the 1000 Å around Hβ . We want an order of magnitude estimate for ϵ so we assume that the continuum is flat. The size of a knot goes as the cube root of the filling factor so small changes in the filling factor will have little effect on the size of the knot. The average radius of the knots as determined in Weistrop *et al.* (2004) is 13.3 pc. This radius was determined from the FUV($\lambda_{central}$1595Å) FWHM. The electron density and proton density were calculated from measurements of [S II] $\lambda\lambda 6717, 6731$ lines from ground based spectra. The procedure is described in the "Electron Temperature and Density" section. The

filling factor can be calculated from

$$\epsilon = \frac{L(H\beta)_{SB99}}{\frac{4\pi}{3} r^3 N_e N_p \alpha^{eff}_{H\beta} h\nu_{H\beta}}$$

and in such a way, $\epsilon \sim 0.1$.

Weistrop *et al.* (2004) find that the sizes (radius) of the knots in NGC 4194 range from $\sim$ 5 to $\sim$ 26 pc and the average radius is $\sim$ 10 pc. The knots in Weistrop *et al.* (2004) numbered 4, 6, 11, 12, 15, 21, 33 and 37 correspond to the knots numbered 6, 3, 2, 1, 8, 9, 11 and 13 in our sample. The radii of the knots in Weistrop *et al.* (2004) mentioned previously by number range from around 5 pc to 9 pc. Hancock *et al.* (2003) find that the average radius of a knot in both NGC 3395 and NGC 3396 is $\sim$7 pc. With observations of NGC 3994 and NGC 3995, Eggers *et al.* (2005) find the radii of knots range from 4-23 pc. Whitmore & Schweizer (1995) find that clusters in NGC 4038/4039 have an average diameter of 18 pc and in NGC 7252 an average radius of 10 pc is observed for the older clusters outside the central gas disk. Globular clusters in the Milky Way and in M87 have effective radii of about 3 pc (Miller *et al.*, 1997). These are all measurements of the sizes of the 'cluster' of stars in a knot. The average size of the knots (H II regions) in NGC 4194 that we measure is 60 pc. The sizes of the H II regions are considerably larger than the volume occupied by the stars, as is to be expected. For instance, Osterbrock (1989) shows that the radius of an H II region surrounding a single O star can be around 5 pc. Our knots likely have a few O stars and perhaps on the order of a hundred B stars.

The H II regions in the knots in NGC 4194 are larger than the typical sizes of Galactic globular clusters. Older globular clusters no longer have H II regions because the young stars that provided the ionizing photons are gone and winds from the hot stars blew out the gas. Weistrop *et al.* (2004) find that at least half of the knots in their sample, including the ones common to our sample, are likely bound and will become globular clusters a few billion years.

Figure 26 is a plot of the radius of the knots with an assumed filling factor of 0.1 against position along the slit. From this plot, it can be seen that the larger knots are found near the center of NGC 4194. Although the sizes we have determined for the knots may not be exact, the trend we see is real. Figure 26 spans 380 MAMA pixels. At the distance of NGC 4194, this corresponds to a linear distance of $\sim$ 1800 pc.

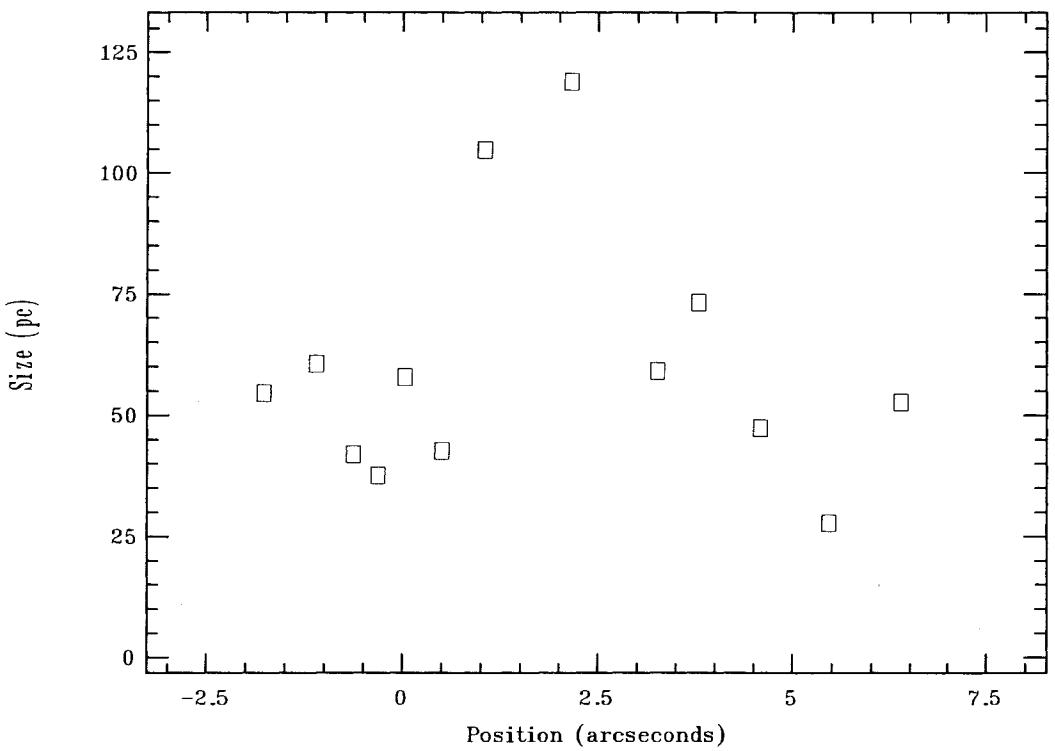

Figure 26 Size vs Position

Ages of the Knots

Comparing our measured EW(Hα+[N II]) and EW(Hβ) with the Starburst99 model, we estimate the ages of the star forming regions (knots) to be $\sim$ 5.5 – 10.5 Myrs. The ages are derived from a model assuming an instantaneous starburst, a

Table 12 Ages of the Knots

Knot	Hα+[N II] age (Myr)	Hα age[a] (Myr)	Hβ age (Myr)
1	6.2	6.4	6.6
2	5.9	6.1	6.1
3	6.0	6.3	6.3
4	6.0	6.2	6.2
5	6.2	6.4	6.2
6	7.0	8.5/10.5	- - -
7	6.2	6.4	6.3
8	5.9	6.1	6.2
9	5.7	6.0	5.9
10	5.5	5.8	5.7
11	5.9	6.2	6.0
12	6.3	6.5	6.4
13	6.3	6.6	6.6
14	6.4	6.6	6.5

[a] assuming [N II] contamination of 40%

Salpeter IMF and solar abundances, as estimated from our data. Starburst99 assumes that all ionizing photons are absorbed. If in fact all the ionizing photons are not absorbed then the model is over estimating the emission line flux and therefore is overestimating the equivalent widths. This means that the ages determined by the model may be an upper limit. The knots may be younger.

Table 12 lists the age determined from the EW(Hα+[N II]), the age determined from the EW(Hα), and the age determined from the EW(Hβ). The ages determined from the EW(Hα) are all slightly older than those determined from the EW(Hα+[N II]) which is what one would expect. There is very good agreement in the ages determined with these equivalent widths. Given the uncertainties in our measurements, the differences in ages are not significant.

Figure 27 is a plot of age against position along the slit. The boxes represent

ages determined from the equivalent width of Hα+[N II] , the plus signs represent the ages determined from the equivalent width of Hα , and the circles represent the ages determined from the equivalent width of Hβ . From this plot it can be seen that the older knots are at the slit center and the outer edges. The youngest knots are found just north and south of the slit center. Given the uncertainties in the Starburst99 model, the uncertainties in our flux measurements and the relatively small spread in ages of the knots, it is not clear that this trend is real, but it is suggestive.

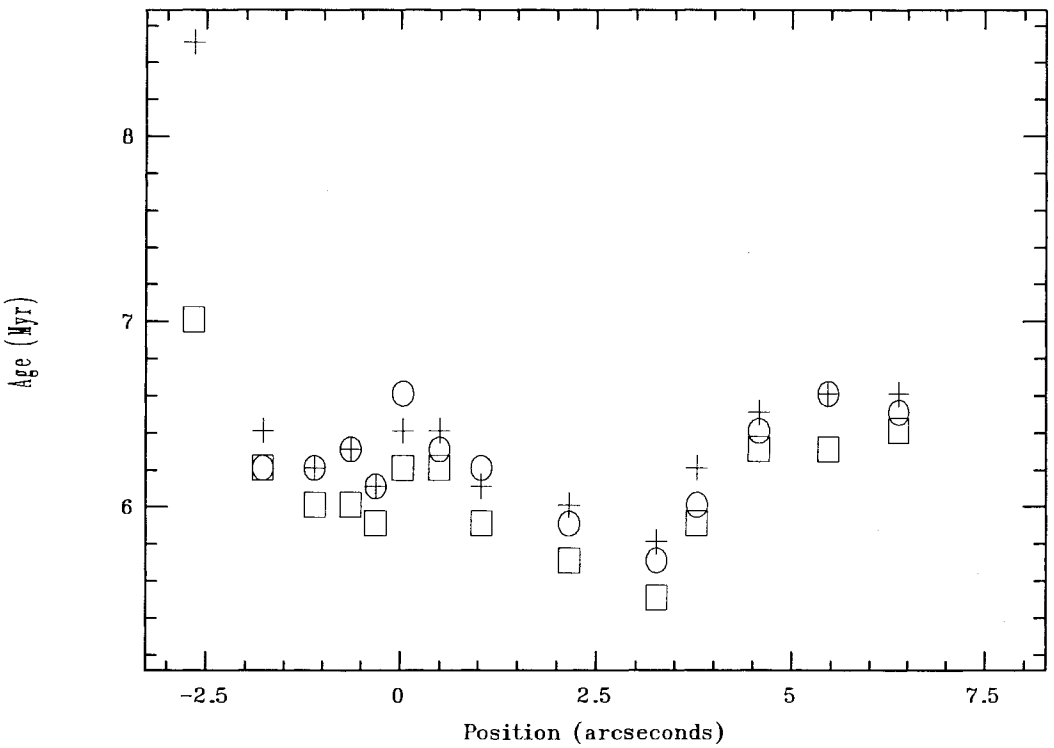

Figure 27 Knot Age vs Position

Weistrop *et al.* (2004) determined that the ages of two thirds of the knots in their sample were less than 20 Myr and that the youngest knots were less than 5 Myr. Four of the knots in Weistrop *et al.* (2004) that correspond to knots in our sample have ages less than 10 Myr. Three of the knots in the Weistrop *et al.* (2004) sample were found to be much older than their counter parts in our sample. The differences

in the ages determined in Weistrop *et al.* (2004) and this study can be attributed in part to differences in the determination of the reddening. The ages determined by Weistrop *et al.* (2004) are also sensitive to their photometry. The FUV/NUV color of the knots span around half a magnitude. A small error in their photometry would result in a vastly different age estimate.

Young knots have also been found in other interacting galaxies. For example, Hancock *et al.* (2003) find that several knots in NGC 3395 and NGC 3396 have ages less than 20 Myr. Some knots are as young as 5 Myr. Eggers *et al.* (2005) reports the ages of 12 knots in NGC 3994 are less than 20 Myr and the ages of 22 knots in NGC 3995 are younger than 10 Myr. In a study on NGC 1741, Johnson *et al.* (1999) found star forming regions as young as a few Myr. Johnson *et al.* (2000) report ages less than 10 Myr for nearly half the knots in He 2-10.

Initial Mass Function and Total Mass

How often are very massive, $\gtrsim 30 M_{\odot}$, O stars formed? Do these massive stars commonly form in the intense environments induced during a merger event or tidal interaction? Do massive stars form at all in regions of intense star formation? Do environments of high Star Forming Efficiency (SFE) preferentially form stars according to a bottom heavy Initial Mass Function (IMF), an IMF with more low mass stars than a standard Salpeter IMF? Do environments of high Star Forming Efficiency (SFE) preferentially form stars according to an IMF truncated at the high mass end? Does the SFR help determine the SFE? In an effort to address these issues, we attempt to fit a model with two different IMFs to our data. One IMF is the standard Salpeter IMF, extending from 1 to 100 $M_{\odot}$ and the other is a Salpeter IMF truncated at an upper limit of 30 $M_{\odot}$. Both of the IMFs used in SB99 are truncated at a low mass limit of 1 $M_{\odot}$ because stars of less mass do not contribute significantly to the

UV spectra. Both of these IMFs are power laws and can be written in this form, $\Phi(M) = cM^{-\alpha}$. For both IMFs $\alpha = 2.35$ and c is the normalization determined by the total mass, 10^6 $M_\odot$ in the case of SB99. The difference in these two IMFs is the range of masses and therefore in the total number of stars in each mass bin. For the convenience of discussion, we will refer to the Salpeter IMF from 1 to 100 $M_\odot$ as SIMF and the Salpeter IMF from 1 to 30 $M_\odot$ as TIMF. We will show that a model assuming the TIMF is a better fit to the data than a model assuming a SIMF.

In order to compare the SB99 model with our data, some preparations needed to be made. The model needed to be converted into the same units as our observations. First, we will describe the preparations made to the UV model and then we will describe the preparations made to the visible model.

The model spectra were redshifted from the rest frame into the observed frame. NGC 4194 has a redshift of 0.00836 (de Vaucouleurs *et al.*, 1991) so the model wavelengths were multiplied by 1.00836. The model luminosities are tabulated in log space with units of ergs s^{-1} $Å^{-1}$. The model luminosities were converted to a linear scale. The model luminosities were divided by $4\pi R^2$ where R is the distance to NGC 4194. This was done to convert the luminosities into fluxes. We assumed that NGC 4194 is at a distance of 39.5 Mpc (Weistrop *et al.*, 2004). The model fluxes then had units of ergs s^{-1} cm^{-2} $Å^{-1}$.

Next the models were reddened. This was done with the IRAF task CALCSPEC. We used the Calzetti, Kinney, & Storchi-Bergmann (1994) starburst reddening law mentioned in the "Reddening Correction" section and the reddening we determined for each knot from the Balmer decrement. The number of magnitudes of reddening was divided by two because we are fitting the continuum and the reddening for the continuum differs from that determined by the Balmer decrement (see the "Reddening Correction" section).

Finally the UV model fluxes were divided by the quantity $1(pix) \times 0.0247(\frac{''}{pix}) \times 0.5('')$. This was done to add the arcsecond squared dependency in the data. The first term is the size of the aperture chosen to define a knot. The reason it is 1 pixel is because the observed flux was averaged over the number of pixels in the aperture. Such an averaged sum is equivalent to a one pixel aperture containing the average value of the flux over the original range. The mass we determine for the knots by fitting the models will be multiplied by the aperture size to give the total mass. The second term is the number of arcseconds per pixel for the detector and is to account for the number of arcseconds in the spatial direction. The third term is the width of the slit in arcseconds and this is to correct for the number of arcseconds of continuum in the dispersion direction. See the "Data Reduction and Calibration" chapter for more information on these corrections.

The UV model Spectral Energy Distribution (SED) includes absorption lines, but does not include Interstellar Medium (ISM) lines. The width of these lines and any possible P-Cygni profiles are determined by the stars' ages and spectral types. Some of these lines are wind features. Most of the absorption lines in our data have an interstellar component or are entirely interstellar. The lines in the model therefore are not as deep as the lines in the data. The model lines were kept as part of the fit because the strength and blue shift of lines such as Si IV λ1403 and C IV λ1550 indicates the relative proportion of stars in the mass range 30-80 $M_{\odot}$ to those in the mass range 10-30 $M_{\odot}$ (Johnson *et al.*, 1999). It is the presence of stars in these mass ranges that we are trying to determine. The quality of the fit of the model to the data will be reduced because of the interstellar components of the observed absorption lines. One could approximate the strengths of these ISM lines from various publications (e.g. de Boer, Koornneef, & Savage (1980)) on R136, the closest example of a starburst. Such a correction would not accurately represent contributions from

the ISM in NGC 4194. The quality of fit will be less without the ISM corrections but the model parameters that result in the best fit will be unchanged because the effect of the continuum is stronger. An ISM correction was not implemented.

The model used for fitting to the visible continuum was prepared in almost the same way as the UV continuum model. The difference was that the model fluxes were instead divided by the quantity $1(pix) \times 0.0507(\frac{''}{pix}) \times 0.5('')$ to add the arcsecond squared dependency to match the observed data. The SB99 model SEDs do not include emission lines. We are trying to fit to the continuum so this is not a concern.

The two IMFs result in model cluster continua that differ in intensity by a factor of around 4 or 5 in the UV. The model cluster continua are very similar in intensity in the visible around Hβ. The SB99 model SEDs assume a total cluster mass of 10^6 $M_\odot$. The knots in our sample are undoubtedly not that mass. If we assume a constant flux to mass ratio then the mass can be used to scale the intensity of the model SEDs. The assumed mass only scales the SED. The IMF assumed will change the shape of the model continuum.

To determine the masses, we fit the visible continua with model SEDs for a wide range of masses. These fits were made assuming an age of 6 Myr, as determined from the EW(Hα) and EW(Hβ) , our measured abundances ($\sim$solar), the measured extinction for each knot, instantaneous star formation and both IMFs. The abundances of the knots, although approximately solar, are not exactly solar. The change in intensity and shape of the model continua with a factor of two change in assumed abundance is much smaller than the difference in intensity resulting from the two assumed IMFs. A chi squared value was calculated for each fit as a measure of the quality of fit. We found that the mass required to best fit a model with both assumed IMFs to the visible spectra was very similar. The masses determined by fitting the visible continuum are ideal because this is where the small mass stars contribute to

the SED and it is the small mass stars that dominate the mass of a star forming knot.

To give one an idea of the distribution of mass by spectral type, we can look at a 10^6 $M_\odot$ cluster with a Salpeter IMF. In such a cluster, O and B stars would make up about 5,000 $M_\odot$, A stars would make up on the order of 45,000 $M_\odot$, the F, G and K stars would make up on the order of 510,000 $M_\odot$, while the M stars would make up on the order of 440,000 $M_\odot$. The F and G, stars dominate the SED between ~3500 Å and 5500 Å as can be seen in Figure 1. Stars of spectral type F and G have masses in the $\sim 1 - 1.5$ $M_\odot$ range. Both of the IMFs we are assuming are integrated from 1 $M_\odot$ and up.

We expected the masses required to fit the model with each IMF to the data to be similar in the visible. A cluster with an IMF truncated at $30M_\odot$ will contain more lower mass stars than one formed according to a SIMF. The luminosity of main sequence stars goes approximately as the cube of the mass. The addition of a few thousand low mass F, and G stars will not impact the SED as much as the mass distribution.

In the UV, the story is different. The model assuming the SIMF will require much less mass to fit the data than will the model assuming the TIMF. The SIMF extends to a higher mass. It is the very high mass stars that contribute to the UV continuum (see Figure 1). A single high mass star will contribute significantly to the UV continuum. Clusters are dominated in mass by small stars but are dominated in UV light by massive stars.

From the model fits to the visible continua, we have only an approximate mass for each of the knots. This method is sensitive, for instance, to reddening and age effects which may not have been totally taken into account.

To help constrain the masses of the knots, we can approximate the total stellar mass independent of model by assuming a SFE. The SFE = M_* / M_{cloud} such that

M_* is the mass of stars resulting from a cloud of mass M_{cloud}. It is a measure of how efficiently matter is converted into stars. The knots in our sample were also observed by Weistrop *et al.* (2004) and were found to be bound. Ashman & Zepf (2001) state that a SFE in the range of 25-50% is necessary to form any bound star cluster. For comparison, the SFE in Giant Molecular Clouds (GMC) in the Milky Way is closer to 0.2% (Ashman & Zepf, 2001). We assume a SFE of 25% and that $M_{cloud} = M_* + M_{gas}$ so that $M_* = \frac{0.25}{1-0.25} \times M_{gas}$ where M_* is the total stellar mass and M_{gas} is the mass of the gas remaining after the stars have formed.

The mass of the gas can be written as $M_{gas} = N_p \times V \times M_p$, where N_p is the number density of protons, V is the volume of the knot, and M_p is the mass of a proton. The number density of protons is equal to the number density of electrons if a pure Hydrogen gas is assumed. See the "Electron Temperature and Density" section for a description of how the electron density was measured. See the "Sizes of the Knots" section to see how the volume was determined.

The masses we determined independent of model (M_{IND}) and the masses we determined from the visible continua fitting agree fairly well. We can say with a small amount of confidence that we know the masses of the knots. With this knowledge of the total stellar mass of the knots we can now decipher the UV continuum fits. The masses of the knots can be found in Table 13. The second column is the mass determined by fitting the UV continuum with a model assuming a SIMF, the third column is the mass determined by fitting a model assuming a TIMF, the fourth column is the mass determined by fitting a model assuming a SIMF to the visible continuum (G430L), the fifth column is the mass determined by fitting a model assuming an TIMF to the visible continuum (G430L), the sixth column is the mass determined independent of model (M_{IND}) by assuming a SFE of 25%, and the last column is the SFE determined with the mass determined from the average of the visible continuum

Table 13 Masses of the Knots

Knot	UV SIMF[a] $10^6 M_\odot$	UV TIMF[b] $10^6 M_\odot$	Vis SIMF[c] $10^6 M_\odot$	Vis TIMF[d] $10^6 M_\odot$	M IND[e] $10^6 M_\odot$	SFE[f] %
1	27	130	19	17	3.5	63
2	0.56	2.9	1.2	1.0	0.97	27
3	0.77	3.9	1.8	1.6	1.4	29
4	0.42	1.7	1.2	1.1	4.1	9
5	0.18	0.90	0.75	0.75	2.9	8
6	- - -	- - -	- - -	- - -	- - -	- - -
7	0.64	3.0	1.5	1.4	1.4	26
8	4.2	21	14	13	21	18
9	1.2	4.7	4.4	4.1	31	4
10	0.32	1.4	1.6	1.4	3.8	10
11	0.50	2.5	3.7	3.4	7.1	14
12	0.64	2.9	3.2	2.9	1.9	34
13	0.63	2.7	1.7	1.6	0.39	59
14	0.10	0.6	0.62	0.58	2.7	7

[a] mass determined from SIMF model fit to UV continuum
[b] mass determined from TIMF model fit to UV continuum
[c] mass determined from SIMF model fit to visible continuum
[d] mass determined from TIMF model fit to visible continuum
[e] mass determined by assuming SFE = 25%, independent of model
[f] SFE determined from <visible mass> / (<visible mass> + gas mass)

fitting and the mass of the gas determined from the proton density.

Knot number 6 in Weistrop *et al.* (2004) has a mass consistent with the mass determined for the corresponding knot, 3, in this study. The rest of the knots have derived masses that differ by a factor of ~ 8. In a few cases the difference is greater. The masses in Weistrop *et al.* (2004) were determined by their photometry. A small photometric error would result in a large change in their determined mass.

The model SEDs assuming both IMFs are quite different in intensity in the UV as is to be expected. Models assuming either IMF can be fit to the UV data with similar chi squares for a particular but different mass. For two of the knots, the mass

required to fit the UV data with a model assuming a TIMF is nearly the same as the mass determined from the visible continua fitting and our determination based on a 25% SFE. For eight of the knots, the mass required to fit the UV data with a model assuming a TIMF is nearly the same as the mass determined from the visible continua fitting. This suggests, that those eight knots are forming according to a IMF truncated at an upper mass of 30 $M_{\odot}$.

Knot 1 is best matched with a model assuming a standard Salpeter IMF. Eight of the knots are best matched with a model assuming an IMF truncated at an upper mass of 30 $M_{\odot}$. In all but four of the knots, a similarity was found, within a factor of $\sim$2, between the mass needed to fit the UV continuum and the mass needed to fit the visible continuum. The mass derived from fitting to the visible and UV continua and M_{IND} agree very well, with a factor of $\sim$ 2, for knot 8 and 12. M_{IND} did not agree with the masses derived from model fitting for knots 1, 4, 5, 9, 10, 11, 13 and 14. If one assumes the total stellar mass of the knots is equal to the average mass needed to fit the visible continua, then the SFE of knots 4, 5, 9, 10, 11 and 14 are $\lesssim$ 15%. This explains why a match with M_{IND} was not found for these knots. For knots 1 and 13, M_{IND} underestimates the mass determined from model fitting. The SFE of these knots may be greater than our assumed 25%. We are unable to say which IMF better fits knots 2, 3, 7, and 13. The determined masses are not different enough to say anything conclusive. Knot 6 was not fit with a model because we were unable to determine a reddening value so could not properly fit a model. We compared the SFE we derived as mentioned above with the SFR determined from the Hα luminosity. We do not find a correlation between the SFR and SFE of the knots. Given the uncertainties in our estimates of the SFR and the SFE, we can not rule out a correlation.

If, as suggested by the fits, the stars in the knots have a truncated IMF, we could

say the following. In regions of intense star formation, the SFE is larger than in GMCs in the Milky Way. We could also say that stars more massive than 30 $M_{\odot}$ did not form. According to the IMF, stars are always formed preferentially small. With an increased SFE there could be a tendency to even more preferentially form small stars and form them to the exclusion of very massive stars.

The conventional wisdom is that small stars are formed first (Herbig, 1962). When the massive stars are formed, their strong stellar winds blow out the gas in the region leaving nothing more to form stars (e.g. Massey & Hunter (1998), Massey (2003)). Perhaps if a region were to more efficiently convert matter into stars, it would produce more than normal numbers of small mass stars. If the small mass stars are made first and most of the material is used to produce them, then less than normal amounts of material would be left to make massive stars. We suggest that in regions where the SFE is high, $\gtrsim$ 15%, stars will form according to a truncated upper mass IMF. A Salpeter mass function truncated at $30M_{\odot}$ is such an IMF. On the other hand, for knots that are very young, $\lesssim$ 10 Myr, perhaps a truncated IMF is well fitted because the most massive stars have not formed yet. We cannot rule out this possibility.

A cluster with no stars more massive than $30M_{\odot}$ will still contain O stars. The most massive stars in such a cluster will still evolve into red super giant stars. Stars with initial masses less than $\sim$ 25 $M_{\odot}$ will not evolve into Wolf-Rayet (WR) stars (Massey, 2003). In a cluster that did not form any super massive stars, there would not be any evidence of WR stars.

One common tracer of WR stars is the He IIλ4686 bump. We do not see an obvious He II Wolf-Rayet bump in any of the knots. The spectra for knots 1 and 4 show weak emission features that may be the WR bump. Knot 1 was best fit by a standard Salpeter IMF so could easily contain or have contained WR stars. We cannot definitely rule out the presence of WR stars in knots 1 and 4. The lack of a

WR bump in the remaining knots implies that there are no WR stars in those knots. If no Wolf-Rayet stars were produced then, by a Conti scenario (Massey, 2003), no stars more massive than $\sim$ 25 $M_{\odot}$ were created in those knots. This is consistent with the idea of the truncated IMF. Another possibility, of course, is that at 6 Myr, the age of the knots, any WR star that may have existed is long gone.

CHAPTER 5

SUMMARY

We present results from an UV and visible wavelength spectroscopic study of the star forming properties of the center of NGC 4194. The spectra were observed with STIS on HST. Fourteen individual knots have been identified and investigated.

From the redshifts of the knots we found that the spectrum of knot 6 was blueshifted relative to the rest of the knots. Furthermore, the UV absorption lines resulting from stellar winds were blueshifted relative to the nebular emission line, Hα, in knot 6. The velocity of the stellar winds in knot 6 is v$\approx$ 1500 km s^{-1} . The weak nebular emission and the presence of strong stellar winds lead us to believe that knot 6 is a bubble.

To correct the measured line fluxes for reddening, we used the Calzetti, Kinney, & Storchi-Bergmann (1994) reddening law. We were unable to de-blend the [N II] $\lambda\lambda$6548, 6583 lines from the Hα line so the entire Hα+[N II] flux was used. We determined the average E(B$-$V)=1.1 mag for the 13 knots. The measured [O III]λ5007/Hβ ratio is consistent with a [N II] $\lambda\lambda$6548, 6583 contamination of approximately 40% in the unresolved Hα+[N II] emission (Osterbrock 1989). Unpublished ground based spectra of NGC 4194 show that the [N II] $\lambda\lambda$6548, 6583 contribution to Hα+[N II] is roughly 40%. If one assumes a contamination of [N II] $\lambda\lambda$6548, 6583 =40% the average E(B$-$V)=0.7 mag. From Figure 22, a plot of E(B$-$V)versus position along the slit, it can be inferred that the extinction is greatest toward the center of NGC 4194.

The metal abundances for 13 knots have been determined with the average of four calibrations using the equivalent widths of UV absorption lines and oxygen emission

line ratios. The C IV λ1550 and Si IV λ1403 equivalent widths were used to determine log(O/H) +12 using the calibrations in Storchi-Bergmann, Calzetti, & Kinney (1994). The emission line ratio of R_{23}=([O II] λ3727 + [O III]$\lambda\lambda$4959, 5007)/Hβ was used to calculate log(O/H)+12 using the calibrations of Zaritsky, Kennicutt, & Huchra (1994) and Kobulnicky, Kennicutt, & Pizagno (1999). The average abundances calculated range from 8.1 ± 0.5 to 8.9 ± 0.1 and are approximately solar (Z=8.92). No obvious gradients in metallicity were found.

The knots in our sample yield a total SFR of ~ 46 $M_\odot$ yr^{-1}using SFR($M_\odot$ yr^{-1})= 7.9×10^{-42}L(Hα) (ergs s^{-1}) (Kennicutt, 1998) and our assumption of a 40% [N II] $\lambda\lambda$6548, 6583 contribution. This is in good agreement with results from Weistrop *et al.* (2004) where the total SFR was determined to be around 30 $M_\odot$ yr^{-1}. Figure 24 is a plot of the SFR versus position along the slit. From this figure it can be seen that the SFR is greatest toward the center of NGC 4194. From Figure 25, a plot of SFR vs metallicity, no correlation between the SFR and abundance can be seen. The total SFR determined by Weistrop *et al.* (2004) was calculated from the total background UV flux in the center of NGC 4194. The agreement of our total SFR with Weistrop *et al.* (2004) suggests that the UV background flux 'escaped' from the knots.

From unpublished ground based spectra of the central region of NGC 4194, the temperature and electron densities were determined. Effective temperatures of $\sim$ 11,000 K and electron densities of ~ 530 cm^{-3} were calculated (Table 11).

The sizes of the H II regions surrounding the stars in the knots were determined from L(Hβ) . The sizes of the knots range from 28 pc to 119 pc when a filling factor of 0.1 is chosen. The sizes are a factor of 2.15 smaller when a filling factor of 1 is chosen. By plotting the size versus position along the slit, we found that the larger knots are found nearer the center of NGC 4194.

Using Starburst99, and the EW(Hα+[N II]) and EW(Hβ) , we estimate the ages

of the star forming regions to be $\sim 5.5 - 10.5$ Myrs. A trend of age increasing with increasing distance from the center of NGC 4194 was found. Given the uncertainties in our flux measurements and the relatively small spread in the ages, this trend may not be real.

By fitting a SB99 model with two different IMFs to the visible and UV continua, we find that eight knots may have formed with a Salpeter IMF truncated at an upper cutoff mass of 30 $M_{\odot}$. By fitting SB99 model SEDs to the visible spectra, we were able to approximate the masses of the knots. Using this approximate mass and the mass of the gas determined from the electron density, we find that the SFE of half of the knots is greater than 15% (Table 13).

The knots in our sample were determined to be bound by dynamical time calculations and escape velocity approximations (Weistrop *et al.*, 2004). We determine the dynamical time of the knots using the sizes determined in Weistrop *et al.* (2004) and our masses and find that in all cases the knots are bound. An SFE in the range of 25% - 50% is necessary to form bound star clusters (Ashman & Zepf, 2001). The SFEs we derived for several of the knots are smaller than the range needed to form bound objects but are orders of magnitude larger than the 0.2% found in GMCs in the Milky Way. Considering the uncertainties in our SFE derivation, we find that our results are consistent with the knots being bound. The knots in our sample are bound and very young. They have masses ranging from half to several million solar masses. It is likely that these knots are the precursors to globular clusters.

REFERENCES

Ashman, K. M. & Zepf, S. E. 2001, AJ, 122, 1888

Ashman, K. M., & Zepf, S. E. 1992, ApJ, 384, 50

Calzetti, D., Kinney, A. L., & Storchi-Bergmann, T. 1994, ApJ, 429, 582

Conti, P. S. 1976, MSRSL, 9, 193

Conti, P. S., & Vacca, W. D. 1994, ApJ, 423, L97

de Boer, K. S., Koornneef, J., & Savage, B. D. 1980, ApJ, 236, 769

Deharveng, J. M., Sasseen, T. P., Buat, V., Bowyer, S., Lampton, M., & Wu, X. 1994, A & A, 289, 715

Demoulin, M. H. 1969, ApJ, 156, 325

de Vaucouleurs, G., de Vaucouleurs, A., Corwin, H. G., Jr., Buta, R. J., Paturel, G., & Fouqué, P. 1991, Third Reference Catalogue of Bright Galaxies (Berlin: Springer)

Eggers, D., Weistrop, D., Stone, A., Nelson, C. H., & Hancock, M. 2005, AJ, 129, 136

Hancock, M., Weistrop, D., Eggers, D., & Nelson, C. H. 2003, AJ, 125, 1696

Heckman, T. M., Robert, C., Leitherer, C., Garnett, D. R., & van der Rydt, F. 1998, ApJ, 503, 646

Herbig, G. H. 1962, ApJ, 135, 736

Hill, J. K., *et al.* 1992, ApJ, 395, L37

Johnson, K. E., Leitherer, C., Vacca, W. D., & Conti, P. S. 2000, AJ, 120, 1273

Johnson, K. E., Vacca, W. D., Leitherer, C., Conti, P. S., & Lipscy, S. J. 1999, AJ, 117, 1708

Kennicutt, R. C. 1998, ARAA, 36, 189

Kewley, L. J., Geller, M. J., Jansen, R. A., & Dopita, M. A. 2002, AJ, 124, 3135

Kinney, A. L., Bohlin, R. C., Calzetti, D., Panagia, N., & Wyse, R. F. G. 1993, ApJS, 86, 5

Kobulnicky, H. A., Kennicutt, R. C., & Pizagno, J. L. 1999, ApJ, 514, 544

Kroupa, P. 2002, Science, 295, 82

Kudritzki, R. P., & Puls, J. 2000, ARAA, 38, 613

Leitherer, C.,*et al.* 1999, ApJS, 123, 3

Massey, P. 2003, ARAA, 41, 15

Massey, P., & Hunter, D. A. 1998, ApJ, 493, 180

McCall, M. L., Rybski, P. M., & Shields, G. A. 1985, ApJS, 57, 1

McGaugh, S. S. 1991, ApJ, 380, 140

Meurer, G. R., Heckman, T. M., Leitherer, C., Kinney, A., Robert, C., & Garnett, D. R. 1995, AJ, 110, 2665

Miller, B. W., Whitemore, B. C., Schweizer, F., & Fall, S. M. 1997, AJ, 114, 2381

Osterbrock, D. E. 1989, Astrophysics of Gaseous Nebulae and Active Galactic Nuclei (Mill Valley, CA: University Science Books)

Prinja, R. K., & Barlow, M. J. 1990, ApJ, 361, 607

Reichen, M., Kaufman, M., Blecha, A., Golay, M., & Huguenin, D. 1994, A & AS, 106, 523

Schweizer, F., Miller, B. W., Whitmore, B. C., & Fall, S. M. 1996, AJ, 112, 1839

Shaw, R. A. & Dufour, R. J. 1995, PASP, 107, 896

Storchi-Bergmann, T., Calzetti, D., & Kinney, A. L. 1994, AJ, 429, 572

Weistrop, D., Eggers, D., Hancock, M., Nelson, C. H., Bachilla, R., & Kaiser, M. E. 2004, AJ, 127, 1360

Whitmore, B. C. 2003, in Space Telescope Science Inst. Symp. Series 14, A Decade of Hubble Space Telescope Science, ed. M. Livio, K. Noll, M. Stiavelli (Cambridge: Cambridge Univ. Press), 153

Whitmore, B. C., Zhang, Q., Leitherer, C., Fall, S. M., Schweizer, F., & Miller, B. W. 1999, AJ, 118, 1551

Whitmore, B. C., & Schweizer, F. 1995, AJ, 109, 960

Whitmore, B. C., Schweizer, F., Leitherer, C., Borne, K., & Robert, C. 1993, AJ, 106, 1354

Woodgate, B., E. *et al.* 1998, PASP, 110, 1183

Zaritsky, D., Kennicutt, R. C., & Huchra, J. P. 1994, ApJ, 420, 87

VITA

Graduate College
University of Nevada, Las Vegas

Mark Hancock

Local Address:
1100 S. Buffalo Dr. Apt #145
Las Vegas, NV 89117

Degrees:
Bachelor of Science, Merged Physics and Astronomy, 1998
Northern Arizona University

Master of Science, Physics, 2001
University of Nevada Las Vegas

Dissertation Title: A Spectroscopic Study of the Star Forming Properties of the Center of NGC 4194

Thesis Committee:
Chairperson, Dr. Donna Weistrop, Ph. D.
Committee Member, Dr. Lon Spight, Ph. D.
Committee Member, Dr. Stephen Lepp, Ph. D.
Graduate Faculty Representative, Dr. Carl Reiber, Ph. D.